Hydrological Processes

WILEY

RESEARCH ARTICLE OPEN ACCESS

Montane Seasonal and Elevational Precipitation Gradients in the Southern Rockies of Alberta, Canada

Celeste Barnes[1] | Ryan J. MacDonald[2] | Chris Hopkinson[1]

[1]Department of Geography and Environment, University of Lethbridge, Lethbridge, Alberta, Canada | [2]MacDonald Hydrology Consultants Ltd, Cranbrook, British Columbia, Canada

Correspondence: Celeste Barnes (celeste.barnes@uleth.ca)

Received: 12 February 2024 | **Revised:** 23 December 2024 | **Accepted:** 6 January 2025

Funding: This research was funded via the following grants: Alberta Research Capacity Program and Canada Foundation for Innovation (grant: 32436); Alberta Environment and Parks (grant: 19GRAEM26); Natural Sciences and Engineering Research Council of Canada, Discovery Grant (2017-04362); and the Alberta Innovates, Energy, and Environment Solutions, the Water Innovation Program (grant: E323726).

Keywords: Canadian Rocky Mountain Eastern Slopes | elevational precipitation gradients | mountain precipitation | seasonality | SWE | water resource management

ABSTRACT

Modelling precipitation inputs in mountainous terrain is challenging for water resource managers given sparse monitoring sites and complex physical hydroclimatic processes. Government of Alberta weather station uncorrected and bias-corrected precipitation datasets were used to examine elevational precipitation gradients (EPGs) and seasonality of EPGs for six South-Saskatchewan River headwater sites (alpine, sub-alpine, valley). January EPG from valley to alpine sites (730 m elevation difference) using uncorrected precipitation was 19 mm/100 m. Corrected EPG was approximately three times greater (61 mm/100 m). The valley received more precipitation than the alpine (inverse EPG) in late spring and summer. A seasonal signal was present whereby all sites demonstrated 50%–70% lower summertime precipitation relative to winter months, with the greatest seasonal variance at the alpine site. Winter watershed-level spatialized precipitation volume was compared to modelled snow water equivalent (SWE) associated with two late-winter airborne lidar surveys. Uncorrected volumes (2020: 64.0×10^6m^3, 2021: 63.2×10^6m^3) were slightly higher than modelled mean SWE (2020: 51.6×10^6m^3, 2021: 44.2×10^6m^3) whereas bias-corrected (2020: 120.5×10^6m^3, 2021: 119.7×10^6m^3) almost doubled the estimate. Corrected precipitation is assumed closer to the true value. Cumulative sublimation, evaporation and snowmelt losses result in ground-level snowpack yield that deviates from total atmospheric precipitation in an increasingly negative manner. The 2020/2021 simulations suggest wintertime atmospheric precipitation exceeds late-winter snowpack accumulation by up to 57% and 63%, respectively. A loss of 16×10^6m^3 (7%) watershed SWE from the alpine zone was partially attributed to redistribution downslope to the treeline-ecotone. Physical snowpack losses from sublimation and melt, or modelling uncertainty due to precipitation correction and alpine snow-density uncertainties can also contribute to observed discrepancies between in situ SWE and cumulative precipitation. Ignoring bias-correction in headwater precipitation estimates can greatly impact headwater precipitation volume estimates and ignoring EPG seasonality is likely to result in under-estimated winter and over-estimated summer yields.

1 | Introduction

The Alberta Eastern Slopes located in the Canadian Rocky Mountains provide a critical water supply flowing in and through the Saskatchewan River Basin from Alberta to Manitoba (Schindler and Donahue 2006; Alberta Environment 2010). Monitoring precipitation and water yield in the Alberta headwater regions is an important element of regional water resource management and flood hazard assessment. The need for accurate information is increasing (Government of Alberta

Hydrological Processes, 2025; 39:e70061
https://doi.org/10.1002/hyp.70061

Ministry of Environment and Parks 2019) as demands from populations, agriculture, and industry continue to increase (Grinder 2010). The Alberta Agriculture Economy is dependent on seasonal mountain snow melt to fill reservoirs supplying water to an extensive irrigation network (Jean and Davies 2015). Climate change is expected to decrease the water supply from Canadian Rocky Mountain snowpacks (Newton, Farjad, and Orwin 2021) with reduced December through February snowfall (Hale et al. 2023). An earlier onset of spring snowmelt (MacDonald et al. 2012) has been observed with a decreased quantity of snow water in Canadian April 1 snow surveys (Hale et al. 2023). By the year 2080, global climate models project a shortening of the winter season from approximately 180–120 days across the Alberta Eastern Slopes (Newton, Farjad, and Orwin 2021). Precipitation in mountain regions is difficult to measure due to the influence of complex relief, landcover and associated weather systems (Roe and Baker 2006). A study of an operational snow melt model used in the Colorado, US Rocky Mountains (Meyer et al. 2023) estimated the timing of snowpack depletion to be up to 1 month later than the measured observation. This presents a challenge for reliable management of mountain-sourced water resources.

Mountain precipitation patterns vary seasonally, with air temperature (Daly et al. 2008), and with solid or liquid precipitation type (Mekis et al. 2018). Orographic enhancement is common in mountainous areas (Houze 2012) where ground level precipitation increases with elevation. In general, air flows up the windward side of a mountain, cooling and condensing (Roe 2005; Smith 2019) as it ascends until the air parcel becomes saturated and precipitates out. On this side of the mountain, more precipitation falls as the air parcel is advected upslope (Barros and Kuligowski 1998). Less precipitation falls on the lee side as air descends and warms producing a rain shadow effect (Galewsky 2009). Atmospheric circulation patterns (Smith 1981) and mountain geometry (Rotunno and Houze 2007) also influence air flow. Upper level winds in mountain regions can transport snow many kilometres from the originating cloud to the point where it first encounters land, whereas the transport distance of rain tends to be within a kilometre (Roe and Baker 2006). Air parcels may split and flow around the mountain (Smith 2019) instead of traversing upwards and over. "Feeder/seeder" cloud systems can develop above mountain ridges. Lower-level orographic frontal-system (feeder) clouds (Rutledge and Hobbs 1983) receive precipitation from upper-level (seeder) clouds to produce enhanced precipitation at higher elevations (Haiden and Pistotnik 2009; Mott et al. 2014). In the western Canadian Rocky Mountains, the winter months from November to February consist primarily of solid precipitation (snow) (Shook and Pomeroy 2012) while the fall (September and October) and spring seasons (March–May) are a combination of rain and/or snow as well as increased melt events (Musselman et al. 2021). There has been a decline in winter precipitation in the North American northern Rocky mountains (Musselman et al. 2021; Hale et al. 2023) that has been attributed to changes in the natural variability of the global climate system (Siler, Proistosescu, and Po-Chedley 2019). Precipitation types can also vary spatially during events (Zhang et al. 2017) where rain occurs in valleys and snow at higher elevations in sub-alpine (McCaffrey and Hopkinson 2017) and alpine areas (Marks et al. 2013).

Time series analysis can be applied to recorded precipitation datasets to gain a better understanding of repeating patterns in the data, representing a range of hydrometeorological processes. Time series data can be characterised as being sequential in nature and measured with the same time-step (Box et al. 2015). Four components can be observed in a time series dataset: cycle, trend, seasonality and random variation (Peixeiro 2022). The cycle represents long-term increasing and decreasing patterns in the data. The trend is an increasing or decreasing pattern present within the time series. The seasonality component is a repeating pattern present at the same time interval, for example, daily, monthly and annually. The random variation is noise in the data.

Hydrologic models are used by water resource and flood forecasting managers to distribute precipitation data inputs through space and time for mountain regions. The Alberta River Forecast Centre has operationalised their "Seasonal Water Supply Outlook" and "Flood Forecast Model" workflows using the VIPER Water Supply Forecasting platform (USDA and NRCS 2007) and SSARR (Streamflow Synthesis and Reservoir Regulation) (Zahmatkesh et al. 2019). The Flood Forecast models currently used by the River Forecast Centre are in the process of transitioning to the Raven hydrological modelling framework (Craig et al. 2020). However, the possibility for seasonal variations in elevational precipitation gradient (EPG) are ignored within most models including VIPER, SSARR and Raven. Typically, models used in mountain contexts adopt a constant and fixed EPG value for the entire simulation period (Lo et al. 2011; Caldwell et al. 2015; Craig et al. 2020). Therefore, a key goal of this study is to evaluate and quantify meso-scale EPG variations in space and through time to enable more accurate distributions of precipitation within the mountainous headwater regions of the Oldman River Basin headwaters in Southern Alberta. A secondary goal is to explore the water resources implications of modelling mountain snowpack distributions as a simple function of cumulative precipitation. This second goal is addressed by applying local EPGs to distribute cumulative precipitation across a watershed, then compare these water volumes to spatially-explicit gridded SWE generated from lidar snow depth and nearby density observations.

Precipitation observations are complicated by sensor- and wind-induced biases such as diurnal temperature drift (Campbell Scientific (Canada) Corp. 2011), evaporative losses, snow capping the gauge orifice, precipitation under-catch due to blowing snow (Goodison, Louie, and Yang 1998; Nitu 2010; Rasmussen et al. 2012; Kochendorfer, Rasmussen, et al. 2017) that tend to result in underestimated water volumes if not corrected (Leeper, Palecki, and Davis 2015; Wolff et al. 2015; Pan et al. 2016; Baghapour, Wei, and Sullivan 2017; Ross, Smith, and Barr 2020; Smith et al. 2020). The uncorrected precipitation measurement is assumed to give a smoothened data series (Wright 2024). The corrected precipitation produces an adjusted upper limit modelled estimate based on sensor and wind input variables. Understanding and accounting for sources of uncertainty or bias in precipitation observation data are necessary when estimating point to point gradients, especially when one location might be more prone to bias (such as wind-induced under-catch) than another. Snow water equivalent (SWE) estimates, computed by multiplying snow depth with snow density (Grünewald et al. 2010), can be compared with precipitation (Avanzi et al. 2021). Airborne lidar technology can accurately map mountain digital elevation models (DEM) (Hopkinson et al. 2001; Hopkinson, Hayashi, and Peddle 2009), and a distributed snow depth model (SDM) by subtracting a snow free DEM from a digital snow surface model captured during snow covered conditions (Hopkinson et al. 2004, 2012; Painter et al. 2016). Snow density can be manually sampled at single point locations (Kinar and Pomeroy 2015), estimated, or modelled at larger spatial extents using longer wavelengths electromagnetic spectrum such as synthetic aperture radar (Naderpour, Schwank, and Mätzler 2017; Thakur et al. 2017). Over large areas where lidar sampled snow depth is highly accurate or the depth variance is small, modelled snow density can be a larger source of uncertainty for lidar-derived SWE (Raleigh and Small 2017). The SDM is combined with snow density to compute SWE (Hopkinson et al. 2012; Painter et al. 2016). Over the course of the winter snow season, canopy interception, sublimation, redistribution of snow and melt will alter spatial snowpack characteristics (Pomeroy et al. 1998). Winter precipitation observations represent snow and/or rain that falls at a point location before other processes modify the precipitation input (Kinar and Pomeroy 2015) such as gravity induced redistribution (and/or avalanching processes) (Hancock et al. 2018), wind mobilisation (Li and Pomeroy 1997; Essery, Li, and Pomeroy 1999; Mott, Vionnet, and Grünewald 2018), sublimation (Essery et al. 2003) or melt (Veatch et al. 2009). Mountain snowpack sublimation losses over the winter season can range from 20% to 30% (MacDonald, Byrne, and Kienzle 2009; MacDonald, Pomeroy, and Pietroniro 2010; Sexstone et al. 2018) depending on location, terrain, canopy, and landscape features. Therefore, when aggregated over a large enough area, such that redistribution effects can be ignored or evened out, total cumulative precipitation measurements will exceed in situ snowpack SWE.

The objective of this research is to examine precipitation data in the southern Alberta Eastern Slopes to evaluate:

a. The consistency of EPGs in this region throughout the year, between measurement sites and across different elevation ranges from valley bottom, sub-alpine (which is generally between 1700 and 2200 m above sea level (m.asl) [McCaffrey and Hopkinson 2017]), to the alpine that can be adopted in hydrologic models.

b. How wintertime EPG-derived precipitation volume (V) totals compare with modelled SWE yields from airborne lidar snow depth measurements at a watershed- or mesoscale (approximately 100 km^2).

2 | Data and Methods

2.1 | Study Area

The study area is in the Canadian Rocky Mountains, southern Alberta Rocky Mountain Eastern Slope headwaters. It is on the eastern side of the continental divide, bordering the United States and British Columbia (Figure 1) in the Oldman River Basin. This region is characterised by a continental climate as shown in Belda et al. (2014). Prevailing winds are out of the southwest. Wintertime Chinooks (Burrows 1903) are common in this region, characterised by quickly increasing air temperatures, strong winds and lowering barometric pressures resulting in blowing snow and melt conditions (MacDonald, Pomeroy, and Essery 2018). The Castle River Watershed (Castle) is northwest of Waterton Lakes National Park (Waterton). The University of Lethbridge Artemis Laboratory (ULAL) installed Geonor totalizing precipitation gauges (Campbell Scientific (Canada) Corp. 2011) in Castle and Waterton (Figure 2 a: CMR [Castle Mountain Ridge], b: WFS [Westcastle Field Station], d: Cameron). Alberta Environment and Protected Areas (AEPA) Pluvio totalizing precipitation gauges (OTT Hydromet GmbH 2019) are shown in Figure 2 (c: Akamina, e: Gardiner, f: WC II [West Castle II]) are in close proximity to the ULAL installations.

The CMR Geonor is in the northwestern portion of Castle at an elevation of 2130 m.asl, above the upper limit of the alpine treeline ecotone ATE. The WFS Geonor was installed at 1400 m.asl (Barnes et al. 2020; Barnes and Hopkinson 2022b) within a valley floodplain clearing, 730 m lower and 3.75 km north on the prevailing downwind side of the CMR site (see Table 1).

In September 2017, the Kenow wildfire (Waterton Lakes National Park 2017) destroyed the AEPA Akamina weather station and burnt most of the Cameron Valley. A third ULAL Geonor was installed within Cameron (at the valley bottom) floodplain at 1655 m.asl. An AEPA Pluvio gauge was re-installed at the Akamina site at 1809 m.asl. No live forest canopy is present, as Waterton sites are in the burnt area. Cameron is 1.3 km away from and 154 m lower on the prevailing downwind side of Akamina. The Waterton Akamina site is 321 m lower than the Castle CMR site. Gardiner is an AEPA sub-alpine site, located 7.15 km northwest of CMR and 190 m lower. West Castle II (WC II) is an AEPA valley bottom site located within Castle, 8.5 km southeast of WFS and 133 m higher.

Precipitation gauges located in Castle and Waterton areas are suitable candidates for examining EPGs and seasonality because of their proximity and elevation differences. AEPA headwater precipitation and snow monitoring stations are in sub-alpine or valley bottom locations and do not represent alpine environments (Newton, Farjad, and Orwin 2021). ULAL sites complement the AEPA precipitation measurement network, as CMR is at an alpine elevation while WFS is situated within a valley bottom (Barnes and Hopkinson 2022b). The Cameron valley station is near the AEPA Akamina site but the elevation range between them is less than the Castle site. The Waterton stations are closer in elevation with Cameron at the valley bottom and Akamina in the sub-alpine. The Waterton stations are within treeline, whereas CMR is above treeline. The Gardiner (northeast of Castle) and WC II (within Castle) Pluvio gauge sites may not be in the same prevailing westerly wind field as CMR or WFS but are close by and thus provide additional comparative valley bottom and sub-alpine precipitation observations. In addition to precipitation measurements, Gardiner and WC II are

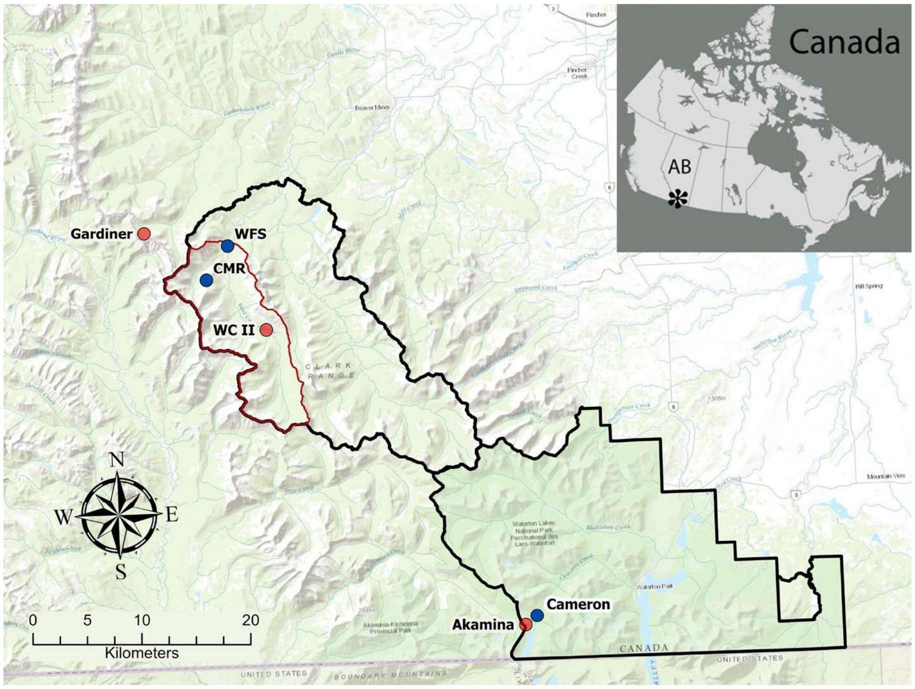

FIGURE 1 | Southwestern Alberta, Rocky Mountain Eastern Slopes region. Castle watershed and Waterton boundaries (black outline), West Castle Watershed (red outline). Blue dots are ULAL gauges, red dots are AEPA precipitation gauges. CMR (Castle Mountain Ridge [2130 m.asl]); WFS (Westcastle Field Station [1400 m.asl]); Akamina (Akamina Pass 2 [1809 m.asl]); Cameron (1655 m.asl); Gardiner (Gardiner Creek [1940 m.asl]); WC II (West Castle II [1533 m.asl]). Inset: Star showing the study location within Alberta, Canada.

AEPA snow monitoring sites, thus providing snow observation datasets to complement the precipitation data used in this study. There are other precipitation gauge stations in Southern Alberta but given the focus of this study is to examine local valley to upper elevation precipitation gradients, the analysis was limited to proximal stations with snow monitoring sites.

West Castle River Watershed (WCW) is a sub-watershed of Castle (Figure 3a) with the outlet located at WFS. It has an elevation range from 1390 to 2630 m.asl (Figure 3b) and an area of ~103 km^2.

2.2 | Data

2.2.1 | Precipitation Gauge Data

Precipitation datasets (observations in mm) used in this analysis were obtained from two different sources: (i) ULAL Geonor gauges https://doi.org/10.20383/102.0551 (Barnes and Hopkinson 2022b); and (ii) publicly available AEPA Pluvio gauge data. ULAL weather stations located in the southern Alberta eastern slopes have sensor- and wind-induced bias corrections applied to the data (Barnes and Hopkinson 2022b; Hopkinson and Barnes 2022). Alberta Climate Information Service (ACIS) publicly available precipitation datasets do not have wind-induced under-catch corrections applied (Goodison, Louie, and Yang 1998; Nitu 2010) since not all AEPA sites record wind speed measurements. The ULAL dataset contains all Geonor precipitation observations for CMR, WFS and Cameron have undergone comprehensive cleaning, smoothing and correction (described in Barnes and Hopkinson (2022b)). Five individual precipitation variables were created that represent the raw measurement (Raw_Precip), ACIS (ACIS_Precip) processed (Wright 2021), additional sensor induced (Leeper, Palecki, and Davis 2015) noise removal (Noise_Precip), removal of over catch resulting primarily from snow (Goodison, Louie, and Yang 1998; Kochendorfer, Nitu, et al. 2017) blowing into the gauge orifice when no precipitation event is in progress (OC_Precip), and a correction for under catch caused by high wind speeds that prevent rain (Pan et al. 2016) or snow (Wolff et al. 2015; Zhang et al. 2015) from entering the gauge orifice during a precipitation event (UC_Precip), as well as the weather observations required to compute the adjusted precipitation variables. Corrected precipitation (Barnes and Hopkinson 2022b) for the WFS and Cameron valley sites differed from the uncorrected measurements by ~−4% to 1%. The CMR alpine ridge adjusted values were ~50% higher than the uncorrected observation with undercatch contributing the most to the correction. This was due to the gauge being in a turbulent/high wind location with mean windspeeds of 8.3 ms^{-1} (~30 kmh^{-1}) and maximum recorded 15-min duration sustained windspeeds exceeding 29.5 ms^{-1} (100 kmh^{-1}) during the wintertime months (October–April). The under-catch adjustment used a catch-efficiency parameter that added missed precipitation to the gauge measurement. The catch-efficiency component for snow was obtained using an exponential empirical formula (Pan et al. 2016) that calculated the wind field above the gauge orifice. Since no wind speed data was available on the precipitation gauge pedestal, wind data from the anemometer located at the top of the adjacent (~10 m horizontal separation) CMR weather station tower was used in this formula. The snow catch-efficiency parameter was most sensitive to the upper threshold value for windspeed. Since the methodology used for the corrections was based on Pan et al. (2016), the upper threshold for windspeed was set to 9.0 ms^{-1} (32.4 kmh^{-1}).

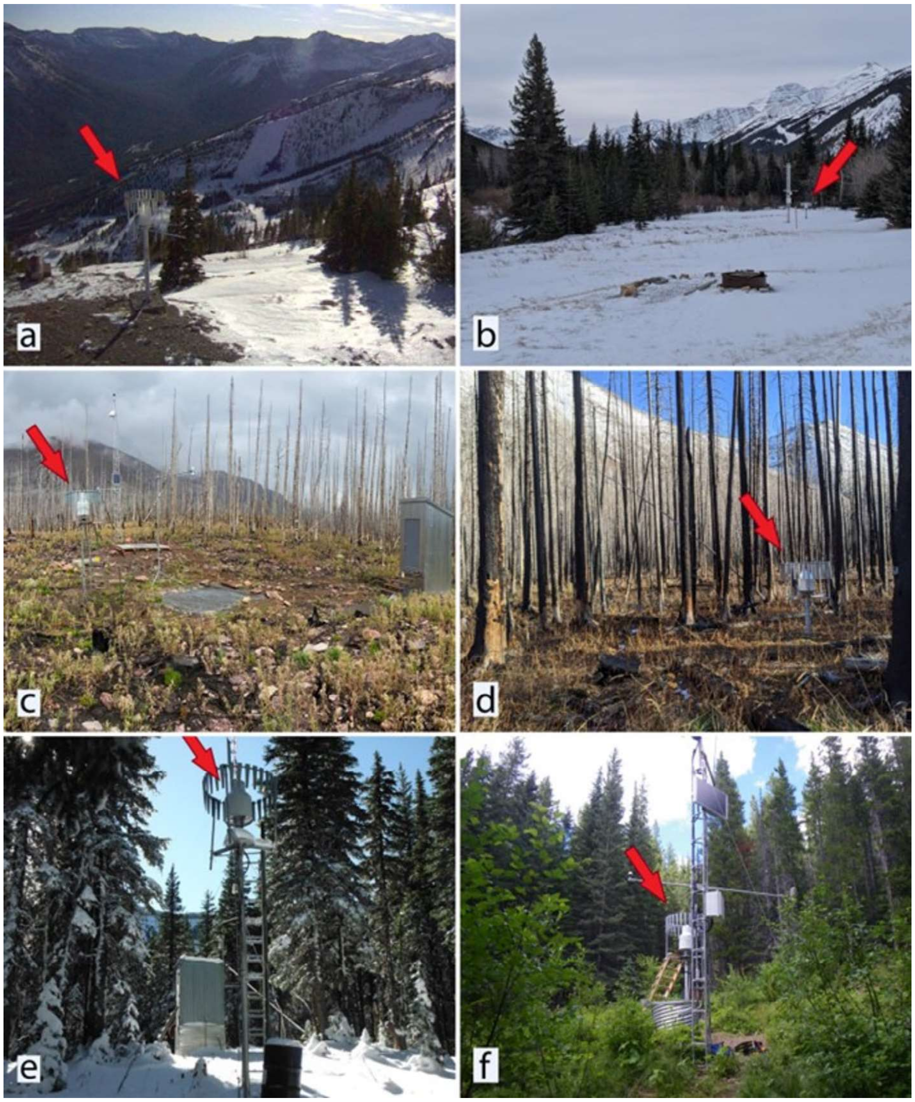

FIGURE 2 | Site characteristics. Paired sites Castle: (a) CMR is located on an alpine ridge with no significant canopy to shelter the gauge, (b) WFS is located in the valley bottom in a large clearing with partial forest canopy. Paired sites Waterton (both sites have dead standing trees): (c) Akamina is in the sub-alpine, within treeline, (d) Cameron is at the valley bottom. AEPA sites in close proximity to CMR and WFS: (e) Gardiner is in a small sub-alpine forest clearing within the treeline, (f) WC II is at the valley bottom within a small forest clearing. Photos (c): Courtesy of Scott Campbell (AEPA), (e and f): Courtesy of https://acis.alberta.ca/weather-data-viewer.jsp.

This value appeared to over amplify the under catch adjustment. A value of 6.5 ms^{-1} (23.4 kmh^{-1}, the wind speed typically used for northern latitudes above 45° and arctic regions (Yang et al. 2005)) was used as the upper limit. The true precipitation under catch adjustment was expected to fall between the lower value (with no wind speed under catch correction) and the upper wind speed threshold correction.

Government of Alberta historical precipitation data are publicly accessible from https://acis.alberta.ca/weather-data-viewer.jsp (ACIS) (Wright 2024) and https://rivers.alberta.ca/ (AEPA) RIVERS "Alberta's River Forecast Centre: Awareness and Communication" system (Alberta Environment and Parks 2019). AEPA public precipitation datasets are cleaned and filtered using a computer algorithm developed by Wright (2021) for sensor noise but do not have wind-induced biases corrections applied (referred to as $\mathrm{P_{UNC}}$). Although two different totalizing precipitation gauges (Geonor and Pluvio) were used, Kochendorfer, Nitu, et al. (2017) found measurements from these sensors to be comparable. The Pluvio gauge uses a proprietary algorithm that is intended to compensate for temperature and wind effects (OTT Hydromet GmbH 2019). However, AEPA Pluvio precipitation data do not have wind-induced bias corrections applied to recorded observations (Nitu 2010). For this study, wind-induced bias corrections were applied to weather station precipitation datasets (referred to as $\mathrm{P_{COR}}$) where data were available to apply such corrections.

ULAL ACIS_Precip (precipitation data from Barnes and Hopkinson (2022b) prior to wind-induced bias corrections) underwent equivalent data cleaning and processing to the AEPA public precipitation data so was considered comparable. However, wind-induced bias can be significant depending on surrounding terrain effects and/or proximity to canopy cover that can shelter the gauge from high wind speeds such as those experienced in the high relief alpine transition environment of

TABLE 1 | Values above the diagonal are distances (km) between each site. Values below the diagonal are elevation differences (m) between sites.

Site	CMR	WFS	Akamina	Cameron	Gardiner	WC II
Distance between sites (km)						
CMR		3.8	43.0	43.2	7.2	7.2
WFS	730		44.3	44.3	7.8	8.5
Akamina	321	409		1.3	50.2	36.0
Cameron	475	255	154		50.3	36.1
Gardiner	190	540	131	285		14.3
WC II	597	133	276	122	407	
Elevation difference between sites (m)						

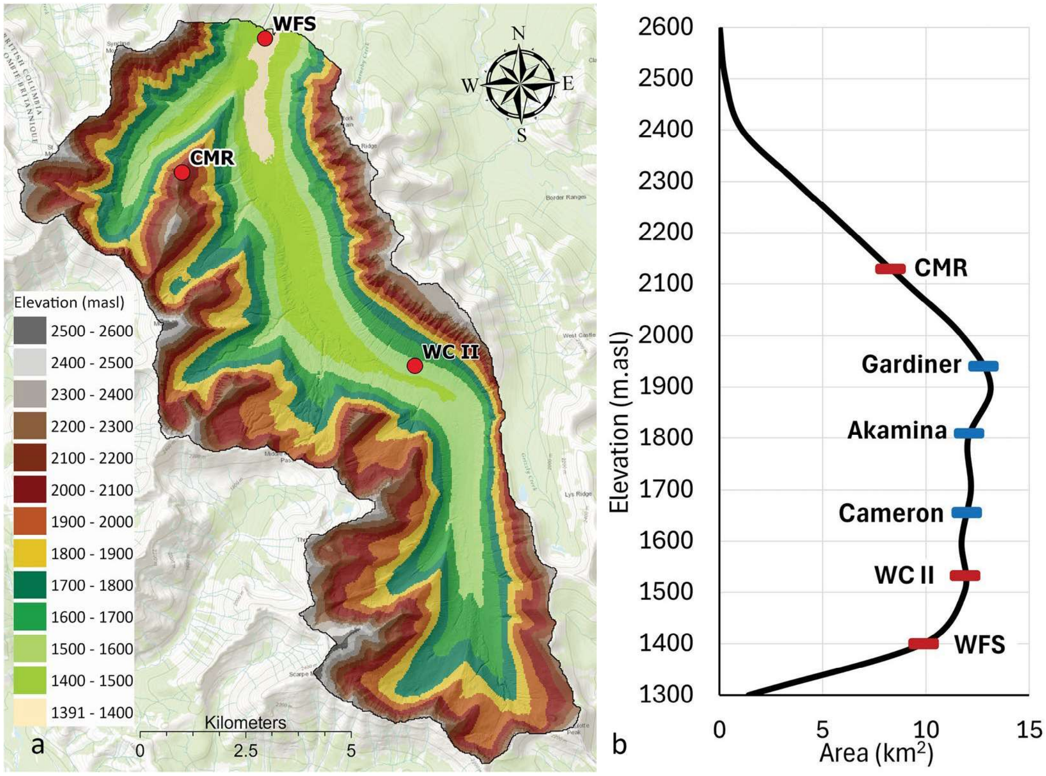

FIGURE 3 | West Castle Watershed (WCW). (a) DEM with shaded relief categorised into 100 m elevation bins. WFS, WC II and CMR are the sites within WCW. (b) Hypsometric curve showing the area per elevation bin. WFS (1400 m.asl), WC II (1533 m.asl) and CMR (2130 m.asl) are identified with red markers. The sites that are not within WCW have been added to the hypsometric curve so all elevations could be listed as a point of reference. Cameron (1655 m.asl), Akamina (1809 m.asl) and Gardiner (1940 m.asl), (not within WCW), are identified on the curve with blue markers.

CMR (Lundquist et al. 2015). ULAL P_{COR} (equivalent to "UC_Precip" in Barnes and Hopkinson (2022b)) data were compared with P_{UNC} data to quantify the potential magnitudes of under-estimation due to wind-induced bias. P_{COR} was not computed for Cameron prior to October 2019 due to local wind speed data being unavailable. Wind data collected at the AEPA Akamina site were used to apply precipitation corrections equivalent to ULAL P_{COR} data. Quality control corrections could not be applied to AEPA Gardner and WC II precipitation since wind data were not available at these sites. ULAL CMR, WFS, Cameron and AEPA Akamina datasets were aggregated to a monthly timestep. General statistics (mean and standard deviation [StDev]) and a linear regression R^2 matrix were computed to examine how sites relate to each other. All ULAL and AEPA datasets were aggregated to cumulative quarterly timestep (Fall: Oct/Nov/Dec; Winter: Jan/Feb/Mar; Spring: Apr/May/Jun; Summer: Jul/Aug/Sep) precipitation for comparative purposes.

P_{UNC} data were expected to produce lower estimates of EPG due to the systematic under-estimate of absolute precipitation. In Barnes and Hopkinson (2022b), the WFS and Cameron (valley bottom sites) experienced small precipitation (P_{UNC} vs. P_{COR}) adjustment ranging from ~ −4% to 1%, whereas CMR (alpine ridge) displayed a ~49% (P_{UNC} vs. P_{COR}) increase in precipitation following corrections for under-catch. However, these P_{UNC} data are used in the analysis presented because others may compute

EPG using publicly available records that have not been corrected or quality controlled. P_{COR} is expected to provide estimates of precipitation and EPG that are closer to true absolute values but given under-catch bias correction is modelled, these data likely contain a greater proportion of overall propagated uncertainty. ULAL P_{UNC} datasets were used to facilitate EPG comparisons with AEPA P_{UNC} data. Both P_{UNC} and P_{COR} datasets were used to examine the range of potential EPG estimates. The study period for CMR, WFS, Gardiner, and WC II was from October 2017 to September 2021. The study period for Cameron and Akamina was from October 2018 to September 2021.

2.2.2 | Snowpack Data

Two airborne lidar surveys flown by ULAL over WCW occurred on 5 March 2020 and 4 March 2021. SDMs were created as described in Barnes and Hopkinson (2022a). Lidar derived DEM uncertainty typically ranges from 0.025 to 0.060 m (Goulden et al. 2016) in regions with low relief and 0.08 m in mountain areas (Painter et al. 2016). A WCW DEM from airborne lidar data collected in July 2020 was used to calculate area per 100 m binned elevation range. The snow depth range for each bin was quantified using the SDM mean depth ± one standard deviation (StDev).

Snow density was computed from AEPA monthly snow depth and SWE field measurements (Pickering 2018) in the Alberta Eastern Slopes headwater region that were sampled within 5 days either side of the first of each month. Akamina, Gardiner, South Racehorse Creek (SRHC) and West Castle II (WC II) field sampling (see Appendix A for additional AEPA field sampling information) data from 1980 to 2021 are available from AEPA https://rivers.alberta.ca/ (Alberta Environment and Parks 2019). AEPA field snow sampling measurements collected at all four sites for the beginning of March from 1980 to 2021 coincide with the dates of both 5 March 2020 and 4 March 2021 SDMs. Snow density was computed using SWE divided by snow depth for each observation in the sample set and expressed as the percentage of standard liquid water equivalent instead of kg/m^3. This approach was used to derive SWE estimates by multiplying snow depth by snow density for each elevation bin. In this study, a snow density range has been assumed using a simple aggregation of observed field samples from the long-term March 1 Government of Alberta historic record. This bracketed snow density approach is expected to result in an amplified range of uncertainty. AEPA field snow sampling is completed at valley to sub-alpine elevations. Snow density increases with elevation (Mizukami and Perica 2008), however, no sampling occurs in the alpine so density is unknown in these higher elevations. Given the variability of snowpack depths in the alpine (ranging from scoured to several metres, see Appendix B for more information on snowpack variability), wind loading (Mott, Vionnet, and Grünewald 2018), and gravity redistribution (Deems et al. 2015), snow density will be highly variable in the alpine. This simplified empirical approach was chosen because a more physically-based density model requires more data and in depth analysis, which is beyond the scope of the presented analysis. In this case, the same snow density range was adopted for all elevation bins using the mean ± one StDev. The March 2020 and 2021 SDM collections were coincident with AEPA field depth and density observations that were within the mean ± one StDev range of the complete 1980–2021 sample set, indicating that these sample sets represent typical late winter snowpack conditions. Airborne lidar snow depth was combined with snow density observations of "mean − one StDev", mean, "mean + one StDev" to compute the range of lidar derived SWE. SWE was estimated for each elevation bin for the same range of snow density using Equation (1):

$$SWE_{elev\_bin} = snow\_depth_{elev\_bin} \times snow\_density \tag{1}$$

2.3 | EPG

EPGs were calculated for both the P_{UNC} and P_{COR} datasets for two sets of paired sites: (1) Castle, CMR (Figure 2a, upper) and WFS (Figure 2b, lower); and (2) Waterton, Akamina (Figure 2c upper) and Cameron (Figure 2d lower) using Equation (2):

$$EPG = \frac{\left(P_{upper} - P_{lower}\right)}{\left(\frac{Elev_{upper} - Elev_{lower}}{100}\right)} \tag{2}$$

where P_{upper} is precipitation from the gauge at the higher elevation ($Elev_{upper}$), P_{lower} is the precipitation from the gauge at the lower elevation ($Elev_{lower}$). A 7-day moving average (MA) was used to smooth the EPG time series. The monthly EPG_{UNC} was calculated using P_{UNC} monthly means from WFS to each of CMR, Gardiner, Akamina, Cameron and WC II.

2.4 | Precipitation Time Series Components

The P_{UNC} monthly datasets were used to explore seasonal variations across the six sites since P_{COR} data were not available for Gardiner and WC II. P_{UNC} observations were sufficient, as accurate absolute magnitudes of precipitation or EPG are not required to explore temporal patterns, provided relative quantities do not vary systematically by site through time. Monthly means and a linear regression matrix were computed for the six sites.

A time series analysis (Box et al. 2015; Peixeiro 2022) was used in this study where each gauge site was sub-divided into three of the four components of seasonality, trend and random variance using a multiplicative model (Equation 3). The cyclical and trend components were not used due to the time series being too short.

$$y_t = C_t \times S_t \times T_t \times R_t \tag{3}$$

where y_t is the observed value at timestep t (a monthly timestep was used in this study), S_t is the seasonal component, T_t is the Trend, R_t is the random variation and C_t is the cyclical component.

To extract the seasonality component, the first step is to use a MA based on the number of timesteps (t) within the repeating time interval of the time series. A 12-month MA was computed for each site's time series using Equation (4). The role of the MA is to smooth the time series to obtain the general upward and downward shifts in the data. Since there are an even number of time periods within the repeating time interval, each MA value does not correspond to a month (t). A centred moving average (CMA) is created using Equation (5) to associate a 12-month MA to the correct month (t). The CMA forms the baseline for the time series.

$$\mathrm{MA}_t = \frac{\sum_{i=t-6}^{t+6} y_i}{12} \tag{4}$$

$$\mathrm{CMA}_t = \frac{\mathrm{MA}_t + \mathrm{MA}_{t+1}}{2} \tag{5}$$

Using the CMA, the time series can be divided into each component. The seasonal index (SI) (Peixeiro 2022) is a percentage of how far above or below the computed value is to the CMA (the baseline of the time series). Positive values indicate SI is higher than CMA and negative values mean SI is lower than CMA. SI was calculated for each month in the time series using Equation (6).

$$\mathrm{SI}_m = \left(\frac{\sum_{i=1}^{n} \frac{y_{m(i)}}{\mathrm{CMA}_{m(i)}}}{n} \right) - 1 \tag{6}$$

where m is the month within the year, n is the number of repeating time intervals (i.e., the number of times that month is present in the time series), i is the summation iterator.

2.5 | Comparing Watershed Spatialized Precipitation Volume With Observed Airborne Lidar Snowpack SWE Yield

Cumulative spatialized winter precipitation was compared with lidar estimates of SWE at watershed scale to evaluate winter precipitation redistribution and potential loss following gauge observation. For the purposes of this comparison, a simple linear increase of precipitation with elevation was assumed since the available precipitation data could not support a more sophisticated approach. The winter accumulation period for $\mathrm{P}_{\mathrm{UNC}}$ and $\mathrm{P}_{\mathrm{COR}}$ (total precipitation) started Oct 1 of the previous year and ended on the date of each airborne lidar mission (5 Mar 2020 and 4 Mar 2021). $\mathrm{P}_{\mathrm{UNC}}$ and $\mathrm{P}_{\mathrm{COR}}$ were used to calculate watershed spatialized precipitation V for comparison to WCW modelled SWE. V was calculated using the monthly EPG from WFS to CMR. For the lowest elevation bin ($\mathrm{P}_{\mathrm{elev\_bin}(m,j=1)}$), where j is the jth elevation bin, was calculated using WFS precipitation (WFS $_{\mathrm{P}(m)}$) where m is the month of the year, multiplied by the area of the elevation bin ($\mathrm{area}_{\mathrm{elev\_bin}(j=1)}$). For each subsequent elevation bin (elev_bin (j)), Equation (7) was used to calculate precipitation ($\mathrm{P}_{\mathrm{elev\_bin}(m,j)}$) using EPG for month m to the highest elevation bin.

$$\mathrm{P}_{\mathrm{elev\_bin}(m,j)} = \mathrm{P}_{\mathrm{elev\_bin}(m-1,j)} + \left(\mathrm{WFS}_{\mathrm{P}} \times \left(\frac{\frac{(\mathrm{P}_{\mathrm{upper}} - \mathrm{P}_{\mathrm{lower}})}{\mathrm{P}_{\mathrm{lower}}}}{\left(\frac{\mathrm{Elev}_{\mathrm{upper}} - \mathrm{Elev}_{\mathrm{lower}}}{100} \right)} \right)_m \right) \tag{7}$$

V per elevation bin (j) was calculated using Equation (8).

$$V_{\mathrm{elev\_bin}(m,j)} = \mathrm{P}_{\mathrm{elev\_bin}(m,j)} \times \mathrm{area}_{\mathrm{elev\_bin}(j)} \tag{8}$$

WCW spatialized precipitation volume total (V) for days from Oct 1 to the date of the airborne lidar mission was computed by summing both the calculated area totals for all elevation bins and all months where nm is the number of months used to calculate the total V and jj is the total number of elevation bins, using Equation (9).

$$V = \sum_{\substack{t=1 \text{ to } nm \\ j=1 \text{ to } jj}} V_{\mathrm{elev\_bin}(m,j)} \tag{9}$$

SWE was calculated for each elevation bin ($\mathrm{SWE\_AreaYield}_{\mathrm{elev\_bin}(m,j)}$) using Equation (10).

$$\mathrm{SWE\_AreaYield}_{\mathrm{elev\_bin}(j)} = \mathrm{SWE}_{\mathrm{elev\_bin}(j)} \times \mathrm{area}_{\mathrm{elev\_bin}(j)} \tag{10}$$

WCW SWE yield was computed by summing the calculated area yield for all elevation bins using Equation (11).

$$\mathrm{SWE} = \sum_{j=1}^{jj} \mathrm{SWE\_AreaYield}(j) \tag{11}$$

3 | Results

3.1 | Site Statistics

A linear regression (assessed using R^2 or coefficient of determination) matrix using monthly $\mathrm{P}_{\mathrm{UNC}}$ for CMR, Gardiner, Akamina, Cameron, WC II and WFS is shown in Table 2. The strongest relationship was between the Waterton Akamina and Cameron sites with a R^2 of 0.93. WFS and Cameron had the second highest R^2 at 0.77. The weakest relationship was between CMR and WFS (R^2 of 0.30). Although the distance between these two sites was only 3.5 km, they had the largest elevation difference of 730 m. The R^2 for $\mathrm{P}_{\mathrm{COR}}$ between CMR and WFS was 0.09 as seen in Table 2.

3.1.1 | Site Precipitation Comparisons

The $\mathrm{P}_{\mathrm{UNC}}$ monthly mean, mean annual totals and standard deviations for each site are shown in Table 3. Akamina and Cameron had a three-year time series with most of the first month of the first year missing from the series whereas the other sites had four complete years. CMR had the highest monthly mean precipitation during the winter months of Nov–Mar and the lowest for May, Aug and Sep. Gardiner's mean monthly precipitation was highest among all sites in Oct, Apr, May and Jul. In Jun, WC II had the highest mean monthly precipitation of all the sites. All sites had lowest precipitation in Jul. Overall, mean annual total uncorrected $\mathrm{P}_{\mathrm{UNC}}$ observations vary between ~900 mm and ~1300 mm/year.

$\mathrm{P}_{\mathrm{COR}}$ monthly mean and standard deviation for the proximal and bias-corrected CMR and WFS sites are shown in Table 4. CMR winter precipitation observations almost doubled from 1262 to 2361 mm/year (+87%) due to wind-induced under-catch corrections (Barnes and Hopkinson 2022b). Monthly mean precipitation for CMR was higher during the snow-dominated period of Nov–Mar with a ~260-mm precipitation correction in the months of Dec and Jan. The precipitation was lower in Jul, Aug

TABLE 2 | Linear regression R^2 for P_{UNC} for the complete time series between CMR (alpine, 2130 m.asl), Gardiner (sub-alpine, 1940 m.asl), Akamina (sub-alpine, 1809 m.asl), Cameron (valley, 1655 m.asl), WC II (valley 1533 m.asl), WFS (valley, 1400 m.asl). P_{COR} for the complete time series between CMR, Akamina, Cameron, and WFS.

PUNC					
Site	CMR	Gardiner	Akamina	Cameron	WC II
Gardiner	0.35				
Akamina	0.43	0.60			
Cameron	0.37	0.59	0.93		
WC II	0.37	0.56	0.72	0.69	
WFS	0.30	0.59	0.68	0.77	0.70
P_{COR}					
Site	CMR	Akamina	Cameron		
Akamina	0.29				
Cameron	0.22	0.97			
WFS	0.09	0.57	0.59		

TABLE 3 | P_{UNC} monthly mean and standard deviation (sites listed by highest [m.asl] to lowest [m.asl] elevation) for CMR (alpine, 2130 m.asl), Gardiner (sub-alpine, 1940 m.asl), Akamina (sub-alpine, 1809 m.asl), Cameron (valley, 1655 m.asl), WC II (valley 1533 m.asl), WFS (valley, 1400 m.asl).

P_{UNC} elev (m.asl)	**CMR alpine 2130**		**Gardiner sub-alpine 1940**		**Akamina sub-alpine 1809**		**Cameron valley 1655**		**WC II valley 1533**		**WFS valley 1400**	
Month	Mean (mm)	StDev (mm)	Mean (mm)	StDev (mm)	Mean (mm)	StDev (mm)	Mean (mm)	StDev (mm)	Mean (mm)	StDev (mm)	Mean (mm)	StDev (mm)
Oct	90.5	16.9	111.7	13.6	102.7	14.5	91.4	7.8	106.8	13.7	84.7	11.2
Nov	135.5	52.1	100.1	14.0	104.3	54.5	84.6	40.3	128.4	53.2	90.4	34.6
Dec	166.6	39.4	155.3	20.6	114.5	38.7	93.1	31.6	134.0	31.4	90.4	12.3
Jan	186.9	43.9	97.4	38.1	90.2	18.0	72.5	15.1	52.9	24.6	58.9	11.7
Feb	156.7	53.5	101.2	55.7	81.9	9.1	73.3	7.4	92.1	37.7	92.8	13.1
Mar	106.3	54.9	90.1	28.1	63.7	42.7	58.8	36.7	71.5	42.6	62.3	27.0
Apr	105.9	26.4	121.0	12.3	102.0	34.2	94.4	29.4	93.5	16.1	86.4	8.9
May	79.9	30.5	112.3	32.6	105.0	17.8	104.0	24.9	86.1	24.9	93.6	37.4
Jun	99.5	34.4	107.8	26.8	123.1	42.5	104.7	39.9	126.1	43.4	87.0	28.4
Jul	36.0	26.1	39.1	28.8	26.9	16.6	19.0	12.2	27.7	21.4	35.4	19.1
Aug	44.3	26.6	61.5	27.8	67.8	42.3	59.5	38.3	56.2	38.4	53.9	36.7
Sep	53.9	21.9	81.6	54.0	97.4	50.1	68.0	31.3	70.8	39.9	62.8	33.7
Annual												
Total	1262.0		1179.0		1079.6		923.3		1046.0		898.5	
Min	36.0		39.1		26.9		19.0		27.7		35.4	
Max	186.9		155.3		123.1		104.7		134.0		93.6	

and Sep rain-dominated period, which also showed a smaller level of precipitation correction. WFS had the lowest mean monthly precipitation in Jul. In Aug and Sep, WFS observed greater precipitation than CMR.

3.1.2 | EPG

The monthly EPG_{UNC} is shown in Figure 4a. There is a positive EPG_{UNC} between WFS and CMR during the snow-covered

TABLE 4 | P_{COR} monthly mean and standard deviation for CMR and WFS. "P_{COR}—P_{UNC}" shows the mean monthly difference of the computed corrected precipitation values for CMR and WFS.

Elev (m.asl)	**CMR (alpine) 2130**			**WFS (valley) 1400**		
Month	Mean (mm)	StDev (mm)	Mean (mm) P_{COR}—P_{UNC}	Mean (mm)	StDev (mm)	Mean (mm) P_{COR}—P_{UNC}
Oct	167.0	57.6	74.77	84.7	15.1	−0.31
Nov	267.4	93.8	108.70	95.5	39.8	4.08
Dec	380.7	125.8	261.40	95.9	13.0	5.41
Jan	452.9	103.2	259.88	55.7	9.3	−2.96
Feb	354.4	142.2	157.56	94.6	16.9	−0.11
Mar	214.8	123.4	79.83	63.8	30.0	2.78
Apr	174.2	48.2	58.20	85.3	9.3	−1.62
May	94.5	38.2	18.28	91.2	38.5	−2.99
Jun	109.9	35.3	11.65	86.7	28.4	−0.48
Jul	37.3	27.3	1.70	34.6	19.0	−0.90
Aug	46.1	27.7	1.87	53.9	37.3	0.17
Sep	61.4	21.6	5.79	80.1	41.0	23.50
Annual						
Total	2360.7			922.0		
Min	37.3			34.6		
Max	452.9			95.9		

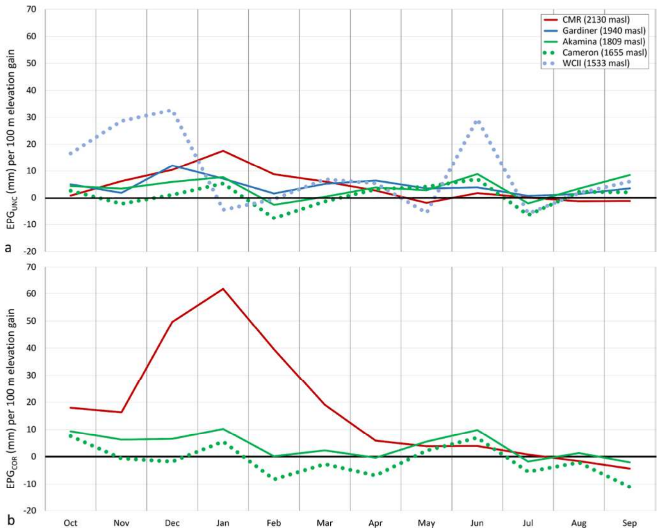

FIGURE 4 | (a) Monthly mean EPG_{UNC} between WFS (1400 m.asl) and all sites (CMR, Gardiner, Akamina, Cameron, and WC II), (b) Monthly mean EPG_{COR} between WFS and sites (Akamina, Cameron, and CMR).

months of Nov to Mar. During the spring melt months of Apr to Jun and the late summer to fall months of Aug to Oct, EPG_{UNC} approaches zero or becomes negative indicating CMR has less precipitation than the lower elevation WFS site. EPG_{UNC} for the Waterton sites (Akamina and Cameron) track closely with WFS with a maximum difference of 6 mm/100 m per month. All sites demonstrated EPG_{UNC} values within the range of −9 mm/100 m per month to 18 mm/100 m per month except for WC II which peaked at 33 mm/100 m for Dec. An inverse EPG_{UNC} (−1 to −7 mm/100 m per month) was evident between WFS and CMR in May, Aug and Sep. Figure 4b shows EPG_{COR} between WFS to CMR, Akamina and Cameron. EPG_{COR} was amplified during the snow-covered months being highest in Jan at 62 mm/100 m per month between WFS and CMR. An inverse EPG_{COR} (−2 to −11 mm/100 m per month) was evident in Aug and Sep between WFS and CMR. There was no consistent precipitation gradient suggesting other synoptic factors influence EPG at a regional scale.

Cumulative daily P_{UNC} (left axis) and 7-day MA EPG_{UNC} (right axis) for the CMR/WFS Castle pair (730 m elevation difference) is shown in Figure 5a. The Castle EPG_{UNC} increased to a daily maximum of 1.5 mm/100 m during winter snow accumulation months. EPG_{UNC} was not as large during the spring melt to summer period with a low of −1.2 mm/100 m. An inverse EPG_{UNC} (Avanzi et al. 2015) occurred in each hydrologic year where the WFS valley site received more precipitation in the summer months than the CMR alpine site. In the 2018–2019 hydrologic year, CMR recorded less precipitation in late winter and spring relative to the previous and subsequent years resulting in a lower overall EPG_{UNC}. The Akamina/Cameron Waterton pair (154 m elevation difference) is shown in Figure 5b. EPG_{UNC} had a maximum of 5.4 mm/100 m that occurred as a result of one rain event at the end of Sep 2019. The EPG_{UNC} was higher in the fall months and lower in the early spring and summer.

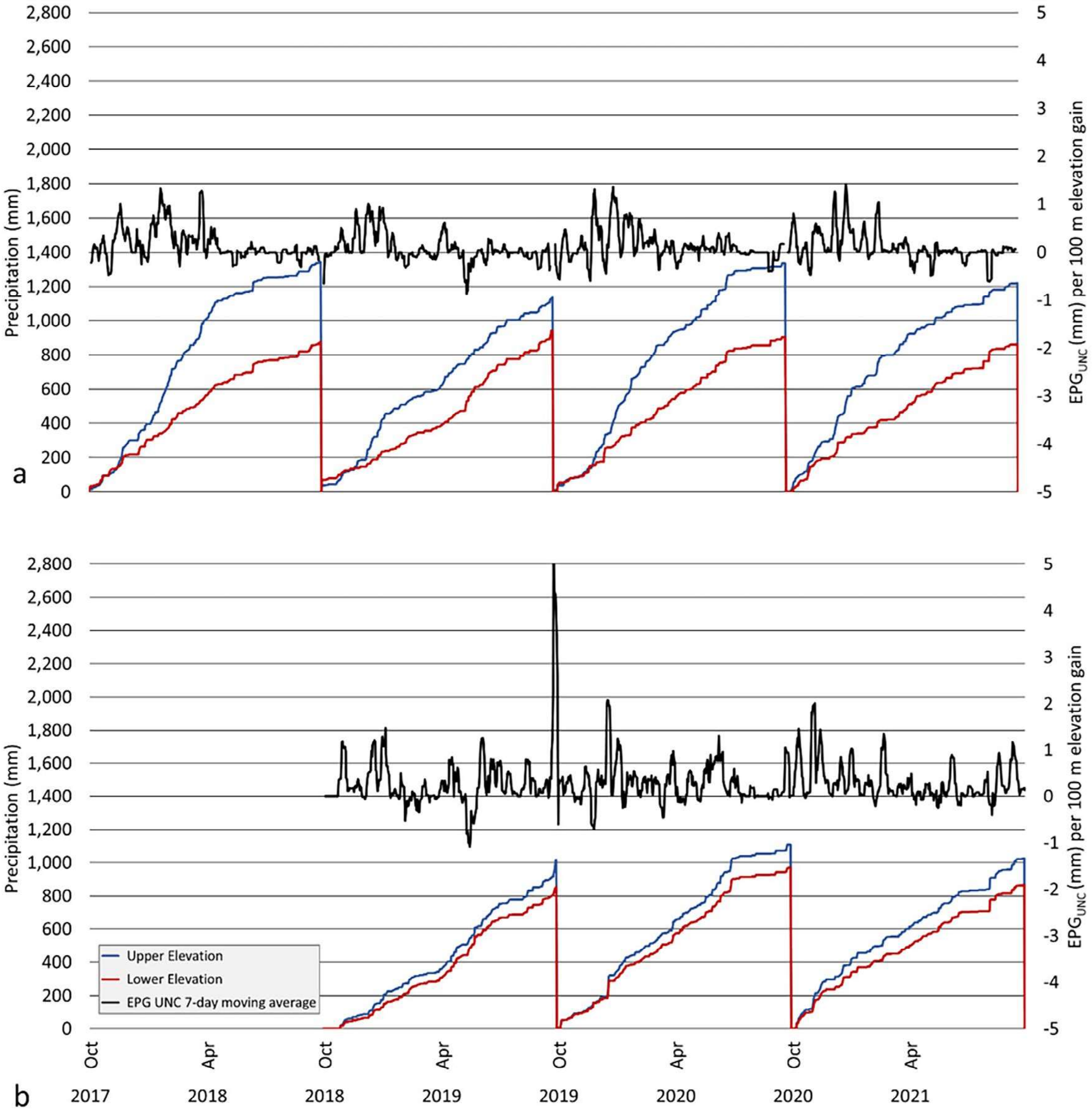

FIGURE 5 | Cumulative daily P_{UNC} (primary axis—left) and EPG_{UNC} (the black line on the secondary axis shown on the right side of the plot is a 7-day moving average) for: (a) Castle sites CMR (blue) and WFS (red) with a 730 m elevation difference. (b) Waterton sites Akamina (blue) and Cameron (red) datasets with a 154 m elevation difference (the series represents the available data).

EPG_{COR} was higher relative to EPG_{UNC} in Castle (Figure 6a) with peak values of 4.2 mm/100 m in the winter months, decreasing in the late spring and summer months. Waterton EPG_{COR} (Figure 6b) had a peak of 2.1 mm/100 m. Generally, Akamina recorded more precipitation than Cameron throughout the entire year.

3.1.3 | Precipitation Time Series

Seasonal (quarterly aggregated P_{UNC}) for all six sites is shown in Figure 7a. For all sites except CMR, quarterly P_{UNC} was higher in the fall and spring. CMR had the highest P_{UNC} in the winter and lowest in the summer months. Figure 7b shows P_{COR} for CMR and WFS for the same periods. CMR P_{COR} was amplified overall and demonstrated the greatest magnitudes in fall and winter. In the summer, the CMR alpine P_{COR} values were below those at valley WFS site.

The seasonality index (Figure 8) was computed for each of the sites. The CMR alpine site received most of its precipitation at the beginning of the winter snow season and less during the remainder of the year, especially May through Sep. Akamina and Cameron seasonal indices were within 6% of each other for all months except Apr, May and Sep. All sites received the least amount of precipitation during the summer months of Jul and Aug.

3.2 | West Castle Watershed Estimated Spatialized Precipitation *V* and Airborne Lidar SWE Water Yield

Airborne lidar derived SDMs are shown in Figure 9. Valley and alpine locations have shallower snow depths. The deepest snowpacks are within treeline (generally between 1700 and 2200 m.asl) sub-alpine regions. Additional information on snowpack conditions at CMR, a sub-alpine site, and WFS can be

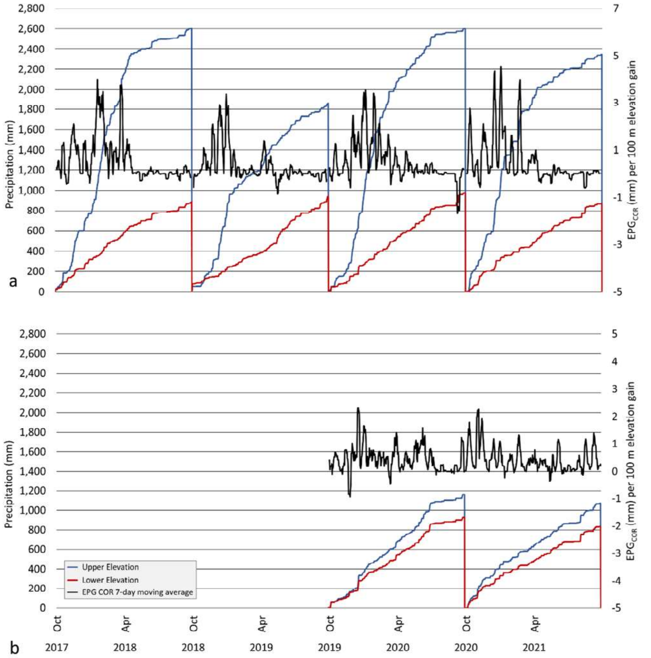

FIGURE 6 | Cumulative daily P_{COR} (primary axis—left) and EPG_{COR} (the black line on the secondary axis shown on the right side of the plot is a 7-day moving average) for: (a) Castle sites CMR (blue) and WFS (red) with a 730 m elevation difference. (b) Waterton sites Akamina (blue) and Cameron (red) datasets with a 154 m elevation difference (the series represents the available data).

seen in Appendix B: WCW Images of snowpack conditions. The AEPA March 1 historic snow density model range was 0.26–0.35 (expressed as a percentage of water equivalent [standard water density is 1000 kg/m^3]).

Estimated WCW precipitation V and lidar-SWE water yields by elevation bin are shown in Table 5. After accounting for EPG and elevation hypsometry, WCW annual spatialized precipitation produces estimated yields of 133.14×10^6 m^3 for V_{UNC} and 175.78×10^6 m^3 for V_{COR} (32% greater). The highest yields were in the elevation range from 1900 to 2000 m.asl (with an area of 13.08 km^2) and produced 14.98×10^6 m^3 for V_{UNC} and 24.89×10^6 m^3 (66% greater) for V_{COR} (Figure 10a). Comparing the winter period V_{UNC} and V_{COR} estimates to the watershed-wide airborne lidar SWE estimate (Figure 10b,c) indicates that the 1900–2000 m.asl elevation range was consistently the most productive for both areal-weighted aggregated precipitation methods as well as the lidar-based SWE estimates. The winter V_{UNC} represented ~58% of annual V_{UNC} and ~70% of annual V_{COR}.

4 | Discussion

There was seasonal variation in daily computed EPG_{UNC} and EPG_{COR} at the Castle and Waterton sites. At the local scale (valley to alpine), annual EPG patterns were generally consistent, with there being enhanced gradients in winter and diminished gradients into spring and summer. EPG_{COR} was amplified in the Castle valley to alpine dataset due to the annual CMR P_{COR} being ~87% greater than the P_{UNC} records, with this enhancement being even greater during winter months due to large under-catch corrections in the windy alpine environment. Similar EPG patterns occurred with the Waterton EPG_{COR} dataset although the magnitudes were smaller, as the Akamina site was below treeline and not as influenced by frequent high wind speeds.

The monthly aggregated P_{UNC} demonstrated pronounced seasonality at all six AEPA (Gardiner, Akamina, WC II) and ULAL (CMR, WFS, Cameron) sites. Precipitation was higher in winter months and lower in summer months for all sites. The seasonality index showed two peaks in the early winter as well as the spring for all sites. Akamina and Cameron had the closest seasonality patterns suggesting they encountered the same local weather patterns. Monthly EPG from WFS to all other sites showed no consistent elevational rate between seasons or annually. WC II showed the highest difference in EPG for the months of Oct/Nov/Dec and Jun. It is well understood that site differences such as differences in the age, proximity and/or density of forest canopy surrounding the gauge can be problematic (Kochendorfer, Nitu, et al. 2017) and introduce uncertainty in precipitation measurements. The Waterton sites have dead standing trees which do not provide additional wind sheltering. Gardiner and WC II are in small clearings with tall conifers to shelter the gauges; however, it is possible for snow intercepted by the forest canopy to blow into the gauges when no precipitation event is in progress. CMR does not have forest canopy to provide additional sheltering of the precipitation gauges. Logistically, alpine monitoring sites (e.g., CMR) are difficult to access and maintain. Wind fields can be turbulent causing equipment failure and precipitation measurement errors. Local atmospheric circulation patterns (Barros and Kuligowski 1998; Roe 2005; Luce, Abatzoglou, and Holden 2013; Collados-Lara et al. 2018; Smith 2019) and mountain geometry (Galewsky 2009; Houze 2012) such as slope and aspect (Daly et al. 2002; Jeong et al. 2020) can affect V and EPG rates (Daly 2002). Lower level precipitation-inducing clouds (Roe and Baker 2006) do not always cover the top of mountain peaks and can precipitate only at lower elevations. In hydrologic modelling, a common practice is to assign an arbitrary EPG rate (MacDonald, Byrne, and Kienzle 2009; Lo et al. 2011; Caldwell et al. 2015; Zahmatkesh et al. 2019; Craig et al. 2020) to spatialize precipitation for the entire simulation. These sources of uncertainty suggest spatial precipitation estimates in mountain environments are unreliable when models are based on a single constant elevation gradient. As seen in the results, there is high variability in EPG spatially and seasonally. When using a consistent EPG to parametrize a model over a large area, precipitation bias will be introduced either spatially or temporally. It is possible to develop a linear estimate based on two points. If there was an intermediate point, there could be a different rate and, in that case, it is likely not a linear gradient Thiessen (1911). It is not practical or cost effective to install a high-density network of these precipitation gauges from valley to alpine.

The spatial yield estimate of annual WCW precipitation for V_{COR} (2020: 120.50×10^6 m^3, 2021: 119.71×10^6 m^3) was almost double V_{UNC} (2020: 63.16×10^6 m^3, 2021: 64.00×10^6 m^3). V_{COR} would be considered an upper bound and V_{UNC} a lower bound of the true *V*. These overall watershed-level yield differences are smaller

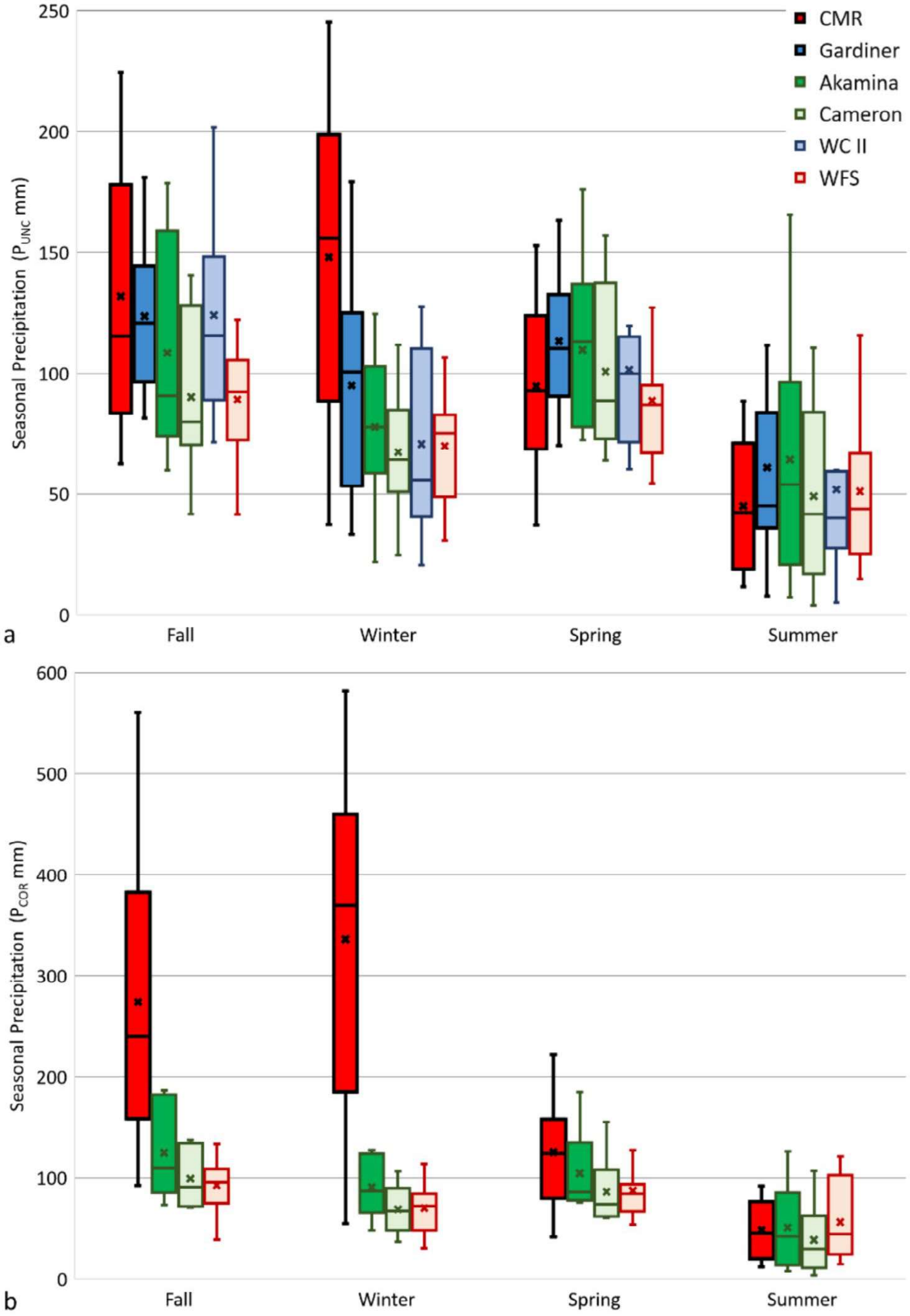

FIGURE 7 | Seasonal precipitation (mm) for (a) 2017–2021 P_{UNC} for CMR, Gardiner, Akamina, Cameron, WC II, and WFS; (b) 2017–2021 P_{COR} for CMR, Akamina, Cameron, and WFS. Box and Whisker, X is mean, bar is median, top and bottom T are the range, coloured box is the interquartile range (quartile 1 to quartile 3). Fall: Oct/Nov/Dec; Winter: Jan/Feb/Mar; Spring: Apr/May/Jun; Summer: Jul/Aug/Sep.

than might be expected from large differences in EPG between methods. However, this is because at valley elevation ranges, P_{UNC} and P_{COR} sensor noise and wind-induced under-catch corrections were negligible (Barnes and Hopkinson 2022b). As elevation increases, P_{UNC} and P_{COR} diverge with differences approximately doubling in the alpine zone but for the watershed, alpine elevations contribute a relatively small proportion of terrain hypsometry.

Comparing V_{UNC} and V_{COR} to airborne lidar-derived late-winter snowpack SWE estimations across the elevation range, it was possible to visualise the potential elevational interaction of precipitation entering a mountainous watershed and the resultant snowpack following redistribution and other modifications. Lidar SDMs show lower snow depths in the alpine and valleys. The deepest snowpacks are within the treeline ecotone (generally between 1700 and 2200 m.asl (McCaffrey and Hopkinson 2017)) sub-alpine regions. V_{COR} exceeded the range of estimated SWE for all elevations. P_{UNC} measurements appear low since the calculated V_{UNC} fell within the range of estimated SWE except for valley and upper alpine elevations. This is unrealistic given observed SWE follows continual snowpack mass losses

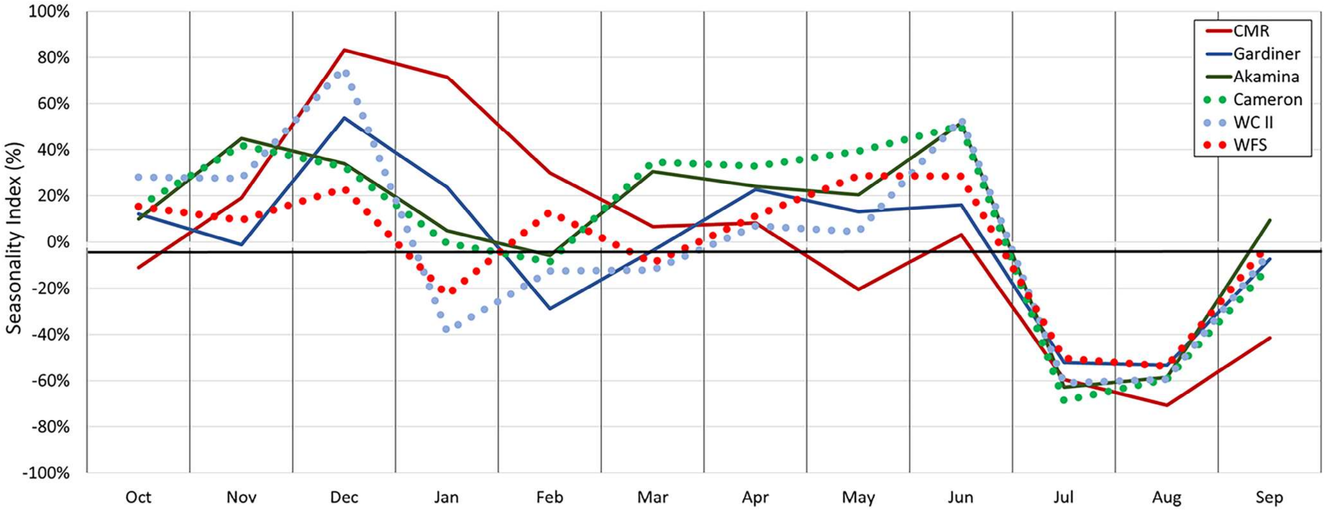

FIGURE 8 | Seasonality index for CMR, Gardiner, Akamina, Cameron, WC II, and WFS. Alpine and sub-alpine sites are a solid line. Valley bottom sites are a dotted line. Positive values indicate SI is higher than CMA and negative values mean SI is lower than CMA.

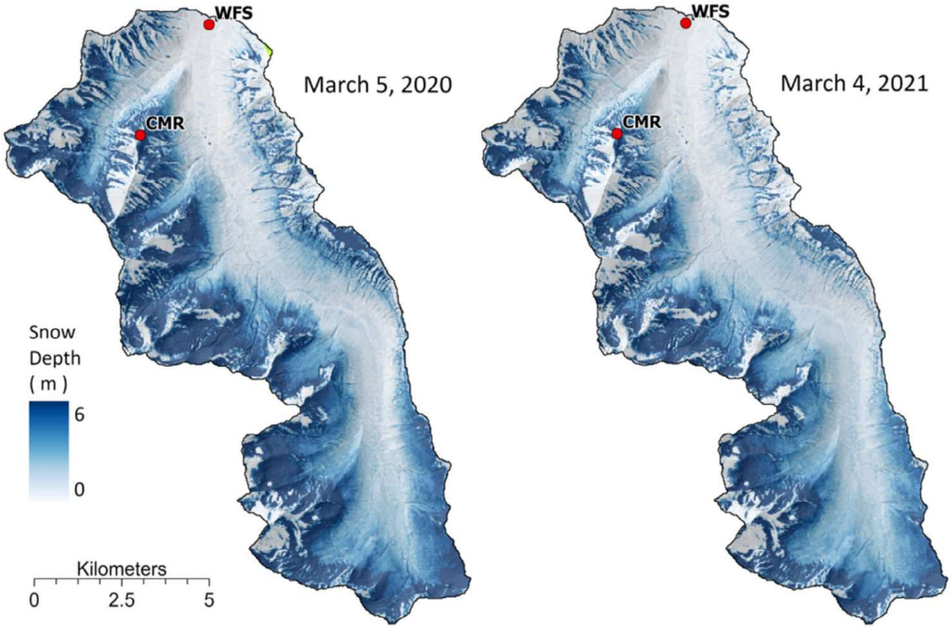

FIGURE 9 | WCW Lidar derived snow depth maps for 5 March 2020 and 4 March 2021.

(Pomeroy et al. 1998) during the winter due to the combined effects of sublimation and melt (Reba et al. 2012; Mott, Vionnet, and Grünewald 2018). Mid to late winter surface SWE should be considerably lower than cumulative V_{UNC}. Consequently, the observed similarity between winter V_{UNC} (mean of $5.3 \times 10^6\,m^3$, StDev of $2.6 \times 10^6\,m^3$) value for all elevation bins and lidar-based watershed scale SWE yield estimates relative to the larger, and subjectively more reasonable V_{COR} (mean of 10.0, StDev of $5.5 \times 10^6\,m^3$) value for all elevation bins estimate, suggests that correcting raw precipitation observations and accounting for seasonal and elevation-based distributions provides an improved range for modelled precipitation-based watershed yield estimates. However, publicly available precipitation records in Canada tend to conform to the P_{UNC} standard and not corrected P_{COR}, so this needs to be considered when such data are used as direct inputs to hydrological models.

The largest areal elevation range in WCW coincides with the lower sub-alpine treeline ecotone from 1700 to 2000 m.asl. This zone also has the greatest snow depths and is the most hydrologically productive zone in the watershed for both V and airborne lidar-modelled SWE (Table 6). Although V was lowest in the alpine zone (above 2200 m.asl), it accounted for 18% (V_{COR}) or 14% (V_{UNC}) of watershed-wide precipitation. The airborne lidar-modelled winter snowpack in the same alpine zone was only 11% of watershed-wide SWE, which is well below the proportions that were estimated to have fallen as snow (whether corrected or not). Aside from differences in lidar SWE and V estimates due to melt and sublimation mass losses, it is a priori expected that alpine zone SWE proportions of overall watershed yield will be lowered relative to atmospheric precipitation-based estimates within the same zone. This is because after precipitation has fallen, gravity (Deems et al. 2015) and wind redistribution

TABLE 5 | West Castle Watershed water yield ($\times 10^6$ m^3) by elevation range. Mean annual yield for V_{UNC}, V_{COR}; water yield for V_{UNC} and V_{COR} from Oct 1 to the date of airborne lidar flight, water yield for Mar 2020 and 2021 airborne lidar SWE.

V and lidar SWE water yield ($\times 10^6$ m^3)									
		Mean annual		**1 Oct 2019–5 Mar 2020**			**1 Oct 2020–4 Mar 2021**		
Area km^2	**Elev range m.asl**	**V_{UNC}**	**V_{COR}**	**V_{UNC}**	**V_{COR}**	**Lidar SWE (range)**	**V_{UNC}**	**V_{COR}**	**Lidar SWE (range)**
11.23	1391–1500	10.07	10.33	4.84	4.80	0.52–3.35	4.70	4.90	0.58–3.23
11.86	1500–1600	11.23	13.24	5.70	7.33	1.17–5.07	5.58	7.34	1.27–4.61
11.69	1600–1700	11.64	15.35	6.21	9.45	1.57–6.86	6.10	9.38	1.52–5.96
12.15	1700–1800	12.70	18.33	7.06	12.13	2.10–9.98	6.96	11.96	1.74–8.55
12.07	1800–1900	13.22	20.58	7.62	14.35	2.35–13.23	7.54	14.09	1.71–11.20
13.08	1900–2000	14.98	24.89	8.91	18.06	2.21–15.68	8.85	17.66	1.53–13.46
11.70	2000–2100	13.97	24.54	8.55	18.37	2.09–14.29	8.51	17.93	1.32–12.37
8.94	2100–2200	11.13	20.52	6.99	15.75	0.85–10.58	6.97	15.34	0.26–9.14
6.15	2200–2300	7.95	15.32	5.11	12.00	0.12–6.63	5.11	11.67	0.00–6.13
3.35	2300–2400	4.50	9.00	2.95	7.18	0.00–3.50	2.95	6.97	0.00–3.07
0.95	2400–2500	1.32	2.74	0.89	2.22	0.00–0.81	0.89	2.15	0.00–0.66
0.26	2500–2630	0.38	0.81	0.26	0.66	0.00–0.23	0.26	0.64	0.00–0.16
103.44		113.09	175.65	65.08	122.28	12.99–90.21	64.41	120.03	9.93–78.55

processes (Grünewald, Bühler, and Lehning 2014) will systematically transport fallen snow to lower elevations.

There is evidence for downward snow redistribution in Table 5, where snow is moving down from the alpine to the high then low treeline zones, respectively. Lidar-based SWE approaches then exceeds the V_{COR} estimates, which is not possible without redistribution from above given the expected in situ snowpack losses due to melt and sublimation. Given no field snow sampling occurs in the alpine zone, snowpack variability from scoured to wind packed drifts can result in underestimated snow density inputs to the lidar-SWE model. Simulated watershed-wide V therefore likely systematically over-estimates the winter SWE yield for upper elevations in the watershed. Uncertainties in P_{COR} can also contribute to the disagreement between V_{COR} and modelled lidar-SWE.

In this part of the Rockies, there are no public precipitation gauges located fully within the alpine zone (Newton, Farjad, and Orwin 2021). This is also a challenge in many other regions of the world (Dozier, Bair, and Davis 2016). This is a concern for spatially distributed water resources assessment, since highly productive elevations are not monitored, meaning seasonal or local to regional EPG variations cannot be ascertained and implemented in models. Therefore, complementary methods, like spatially distributed point-in-time observations of snowpack depth from airborne lidar (Hopkinson et al. 2012; Hedrick et al. 2018) can assist in water resource quantification (Painter et al. 2016) within these headwater mountainous environments.

5 | Conclusions

While public records require correction to provide improved absolute estimates of atmospheric precipitation, inherent spatial variability in precipitation combined with redistribution and snowpack mass loss processes mean that even corrected records can be unreliable for quantifying water yield from mountainous watersheds. This study has shown that precipitation depth covariance in this region weakens rapidly beyond spatial or elevation separations exceeding on the order of ~2 km and ~200 m, respectively. These data suggest spatially representing precipitation gradients to provide reliable water yield estimates is a substantial challenge.

Pronounced seasonality was observed in precipitation data, with the signal at the lower elevation sites being more subdued. Monthly EPG_{UNC} between the proximal WFS and CMR sites confirm the expectation of increased precipitation with elevation during the winter months. An inverse EPG_{UNC} occurred in May, Aug, and Sep. EPG_{COR} from WFS to CMR showed an amplified winter EPG pattern and inverse EPG in Aug and Sep for all sites. Monthly precipitation depths did not increase linearly with elevation between all sites. Since seasonality was observed in the records, there is no stable year-round linear precipitation gradient, and any estimate of montane precipitation across the southwest Alberta headwaters requires a seasonally variable EPG.

An innovative comparison of hypsometric interpolations of winter V_{UNC} and V_{COR} records to two late-winter snowpack datasets

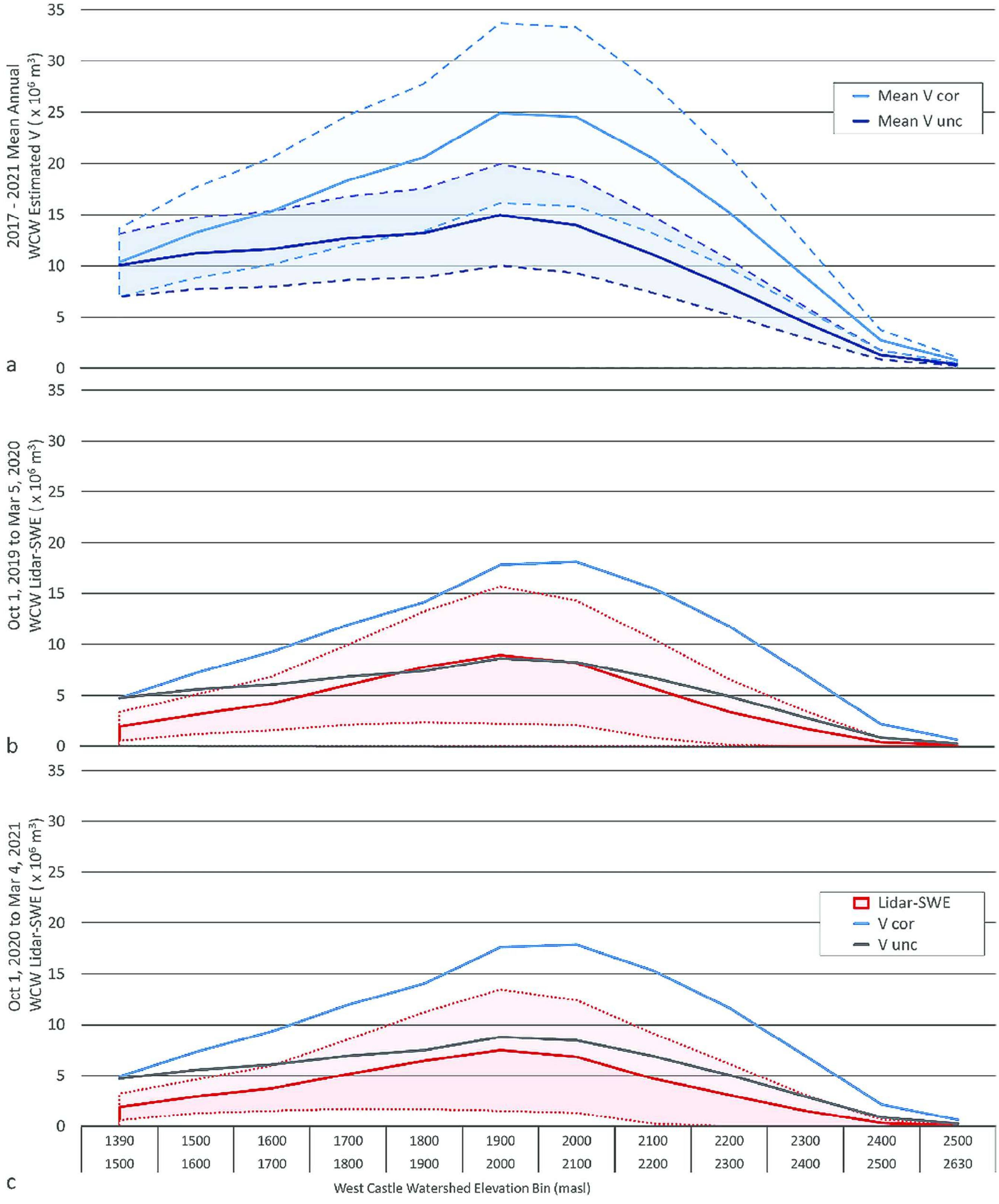

FIGURE 10 | V_{UNC}, V_{COR} and airborne lidar-SWE for the West Castle Watershed. (a) Annual V_{UNC} and V_{COR} (mean ± 1 StDev) 2017–2021, (b) 1 Oct 2019–5 Mar 2020 V_{UNC} and V_{COR}, estimated SWE from 5 Mar 2020 lidar-derived SDM using mean ± 1 StDev snow depth multiplied by mean ± 1 StDev AEPA derived 1980–2021 snow density; (c) 1 Oct 2020–4 Mar 2021 V_{UNC} and V_{COR} and estimated SWE calculated from 4 Mar 2021 lidar derived SDM using mean ± 1 StDev snow depth multiplied by mean ± one StDev AEPA derived 1980–2021 snow density.

TABLE 6 | Estimated annual and mid winter WCW V_{UNC}, V_{COR} and airborne lidar SWE water yield ($\times 10^6$ m^3) by valley (WFS, WCII, Cameron); sub-alpine (treeline generally between 1700 and 2200 m.asl, low treeline: Gardiner, Akamina, high treeline: CMR); and alpine.

	Valley		Low treeline		High treeline		Alpine		
Elevation range (m.asl)	Below 1700		1700–2000		2000–2200		Above 2200		Total
WCW area (km^2)	34.79	(34%)	37.30	(36%)	20.64	(20%)	10.71	(10%)	103.44
Annual V_{UNC}	32.94	(29%)	40.90	(36%)	25.10	(22%)	14.16	(13%)	113.09
Annual V_{COR}	38.92	(22%)	63.80	(36%)	45.07	(26%)	27.87	(16%)	175.65
1 Oct 2019–5 Mar 2020 V_{UNC}	16.75	(26%)	23.59	(36%)	15.54	(24%)	9.21	(14%)	65.08
1 Oct 2019–5 Mar 2020 V_{COR}	21.57	(18%)	44.54	(36%)	34.12	(28%)	22.05	(18%)	122.28
5 Mar 2020 Lidar SWE (mean)	9.28	(18%)	22.77	(44%)	13.91	(27%)	5.64	(11%)	51.60
1 Oct 2020–4 Mar 2021 V_{UNC}	16.38	(25%)	23.35	(36%)	15.48	(24%)	9.21	(14%)	64.41
1 Oct 2020–4 Mar 2021 V_{COR}	21.62	(18%)	43.71	(36%)	33.27	(28%)	21.43	(18%)	120.03
4 Mar 2021 Lidar SWE (mean)	8.59	(19%)	19.10	(43%)	11.54	(26%)	5.01	(11%)	44.24

over the West Castle Watershed did allow a direct comparison of atmospheric precipitation to snowpack accumulation at the gridded (grid cell level) lidar-derived SDM. The March 2020 and March 2021 SDMs show WCW snowpacks were deepest in the sub-alpine and shallow in both the valley and alpine elevations. The most hydrologically productive elevation in WCW for both late-winter spatialized precipitation and airborne lidar-estimated water yield was at treeline elevations between 1700 and 2200 m.asl. Comparing late-winter hypsometric differences between lidar-based SWE and spatially distributed cumulative precipitation, suggests that up to 7% of the total winter-time watershed snow that falls in the alpine zone above 2200 m.asl is subsequently redistributed downwards into treeline elevation zones. Given rainfall infiltration, snowmelt, and sublimation losses can occur during the winter period, mid to late winter snowpack SWE will be lower than cumulative winter season precipitation. Uncertainties in precipitation corrections, and modelled snow density in alpine elevations can also contribute to any observed difference. Spatially-explicit single point in time remote sensing-based estimates of SWE, provide a valuable reference for cumulative wintertime point-based precipitation in mountain water resource simulations.

Acknowledgements

This research was funded via the following grants: Alberta Innovates, Energy, and Environment Solutions, the Water Innovation Program (grant: E323726); Alberta Environment and Parks (grant: 19GRAEM26); Natural Sciences and Engineering Research Council of Canada, Discovery Grant (2017-04362); and the Alberta Research Capacity Program and Canada Foundation for Innovation (grant: 32436). We thank Reed Parsons for assistance with the Geonor installation at the CMR site and Thomas Porter for assistance with the Geonor installation at the WFS and Cameron sites, as well as maintenance at all sites. Alberta Environment and Protected Areas is thanked for assistance with winter maintenance at the Cameron site. We thank Dr. Brandi Newton and the anonymous reviewers for invaluable comments during the revision of this manuscript.

Conflicts of Interest

The authors declare no conflicts of interest.

Data Availability Statement

The raw and processed precipitation and supplemental meteorological datasets are available for download from the Federated Research Data Repository: https://doi.org/10.20383/102.0551 (accessed on 4 May 2022) under Creative Commons Attribution 4.0 International (CC BY 4.0) licence.

References

Alberta Environment. 2010. *Facts About Water in Alberta*. Edmonton, AB: Government of Alberta.

Alberta Environment and Parks. 2019. *Alberta's River Forecast Centre: Awareness and Communication*. Edmonton, AB: Alberta Environment and Parks, Government of Alberta. https://rivers.alberta.ca/.

Avanzi, F., C. De Michele, S. Gabriele, A. Ghezzi, and R. Rosso. 2015. "Orographic Signature on Extreme Precipitation of Short Durations." *Journal of Hydrometeorology* 16, no. 1 (February): 278–294. https://doi.org/10.1175/jhm-d-14-0063.1.

Avanzi, F., G. Ercolani, S. Gabellani, et al. 2021. "Learning About Precipitation Lapse Rates From Snow Course Data Improves Water Balance Modeling." *Hydrology and Earth System Sciences* 25, no. 4: 2109–2131. https://doi.org/10.5194/hess-25-2109-2021.

Baghapour, B., C. Wei, and P. E. Sullivan. 2017. "Numerical Simulation of Wind-Induced Turbulence Over Precipitation Gauges." *Atmospheric Research* 189: 82–98. https://doi.org/10.1016/j.atmosres.2017.01.016.

Barnes, C., and C. Hopkinson. 2022a. "Comparing Mountain Snowpack Depth Model Results From Different Airborne Laser Scanning Flight Path Samples." *Canadian Journal of Remote Sensing* 48, no. 1: 81–92. https://doi.org/10.1080/07038992.2021.1999797.

Barnes, C., and C. Hopkinson. 2022b. "Quality Control Impacts on Total Precipitation Gauge Records for Montane Valley and Ridge Sites in SW Alberta, Canada." *Data* 7, no. 6: 73. https://doi.org/10.3390/data7060073.

Barnes, C., C. Hopkinson, T. Porter, and Z. Xi. 2020. "In-Situ LED-Based Observation of Snow Surface and Depth Transects." *Sensors* 20, no. 8: 2292. https://www.mdpi.com/1424-8220/20/8/2292.

Barros, A. P., and R. J. Kuligowski. 1998. "Orographic Effects During a Severe Wintertime Rainstorm in the Appalachian Mountains." *Monthly Weather Review* 126, no. 10: 2648–2672. https://doi.org/10.1175/1520-0493(1998)126<2648:Oedasw>2.0.Co;2.

Belda, M., E. Holtanová, T. Halenka, and J. Kalvová. 2014. "Climate Classification Revisited: From Köppen to Trewartha." *Climate Research* 59, no. 1: 1–13. https://www.int-res.com/abstracts/cr/v59/n1/p1-13/.

Box, G. E., G. M. Jenkins, G. C. Reinsel, and G. M. Ljung. 2015. *Time Series Analysis: Forecasting and Control*. Upper Saddle River, NJ: John Wiley & Sons.

Burrows, A. T. 1903. "The Chinook Winds." *Journal of Geography* 2, no. 3: 124–136. https://doi.org/10.1080/00221340308985932.

Caldwell, P. V., J. G. Kennen, G. Sun, et al. 2015. "A Comparison of Hydrologic Models for Ecological Flows and Water Availability." *Ecohydrology* 8, no. 8: 1525–1546. https://doi.org/10.1002/eco.1602.

Campbell Scientific (Canada) Corp. 2011. *GEONOR T-200B Series Precipitation Gauge*, 64. Edmonton, AB: Campbell Scientific (Canada) Corp.

Collados-Lara, A.-J., E. Pardo-Igúzquiza, D. Pulido-Velazquez, and J. Jiménez-Sánchez. 2018. "Precipitation Fields in an Alpine Mediterranean Catchment: Inversion of Precipitation Gradient With Elevation or Undercatch of Snowfall?" *International Journal of Climatology* 38, no. 9: 3565–3578. https://doi.org/10.1002/joc.5517.

Craig, J. R., G. Brown, R. Chlumsky, et al. 2020. "Flexible Watershed Simulation With the Raven Hydrological Modelling Framework." *Environmental Modelling & Software* 129: 104728. https://doi.org/10.1016/j.envsoft.2020.104728.

Daly, C. 2002. *Variable Influence of Terrain on Precipitation Patterns: Delineation and Use of Effective Terrain Height in PRISM*, 7. Corvallis, OR: Oregon State University.

Daly, C., W. P. Gibson, G. H. Taylor, G. L. Johnson, and P. Pasteris. 2002. "A Knowledge-Based Approach to the Statistical Mapping of Climate." *Climate Research* 22, no. 2: 99–113. https://www.int-res.com/abstracts/cr/v22/n2/p99-113.

Daly, C., M. Halbleib, J. I. Smith, et al. 2008. "Physiographically Sensitive Mapping of Climatological Temperature and Precipitation Across the Conterminous United States." *International Journal of Climatology* 28, no. 15: 2031–2064. https://doi.org/10.1002/joc.1688.

Deems, J. S., P. J. Gadomski, D. Vellone, et al. 2015. "Mapping Starting Zone Snow Depth With a Ground-Based Lidar to Assist Avalanche Control and Forecasting." *Cold Regions Science and Technology* 120: 197–204. https://doi.org/10.1016/j.coldregions.2015.09.002.

Dozier, J., E. H. Bair, and R. E. Davis. 2016. "Estimating the Spatial Distribution of Snow Water Equivalent in the world's Mountains." *WIREs Water* 3, no. 3: 461–474. https://doi.org/10.1002/wat2.1140.

Essery, R., L. Li, and J. Pomeroy. 1999. "A Distributed Model of Blowing Snow Over Complex Terrain." *Hydrological Processes* 13, no. 1415: 2423–2438.

Essery, R., J. Pomeroy, J. Parviainen, and P. Storck. 2003. "Sublimation of Snow From Coniferous Forests in a Climate Model." *Journal of Climate* 16, no. 11: 1855–1864. https://doi.org/10.1175/1520-0442(2003)016<1855:sosfcf>2.0.co;2.

Galewsky, J. 2009. "Rain Shadow Development During the Growth of Mountain Ranges: An Atmospheric Dynamics Perspective." *Journal of Geophysical Research: Earth Surface (2003–2012)* 114, no. F1. https://doi.org/10.1029/2008JF001085.

Goodison, B. E., P. Y. Louie, and D. Yang. 1998. *WMO Solid Precipitation Measurement Intercomparison*. Switzerland: World Meteorological Organization Geneva.

Goulden, T., C. Hopkinson, R. Jamieson, and S. Sterling. 2016. "Sensitivity of DEM, Slope, Aspect and Watershed Attributes to LiDAR Measurement Uncertainty." *Remote Sensing of Environment* 179: 23–35. https://doi.org/10.1016/j.rse.2016.03.005.

Government of Alberta Ministry of Environment and Parks. 2019. "Knowledge for a Changing Environment: 2019-2024 Science Strategy." Government of Alberta, Ministry of Environment and Parks. open.alberta.ca/publications/9781460142370.

Grinder, B. 2010. "South Saskatchewan River Basin in Alberta Water Supply Study Summary." Alberta Agriculture and Rural Development.

Grünewald, T., Y. Bühler, and M. Lehning. 2014. "Elevation Dependency of Mountain Snow Depth." *Cryosphere* 8, no. 6: 2381–2394.

Grünewald, T., M. Schirmer, R. Mott, and M. Lehning. 2010. "Spatial and Temporal Variability of Snow Depth and SWE in a Small Mountain Catchment." *Cryosphere* 4: 215–225.

Haiden, T., and G. Pistotnik. 2009. "Intensity-Dependent Parameterization of Elevation Effects in Precipitation Analysis." *Advances in Geosciences* 20: 33–38.

Hale, K. E., K. S. Jennings, K. N. Musselman, B. Livneh, and N. P. Molotch. 2023. "Recent Decreases in Snow Water Storage in Western North America." *Communications Earth & Environment* 4, no. 1: 170. https://doi.org/10.1038/s43247-023-00751-3.

Hancock, H., A. Prokop, M. Eckerstorfer, and J. Hendrikx. 2018. "Combining High Spatial Resolution Snow Mapping and Meteorological Analyses to Improve Forecasting of Destructive Avalanches in Longyearbyen, Svalbard." *Cold Regions Science and Technology* 154: 120–132. https://doi.org/10.1016/j.coldregions.2018.05.011.

Hedrick, A. R., D. Marks, S. Havens, et al. 2018. "Direct Insertion of NASA Airborne Snow Observatory-Derived Snow Depth Time Series Into the iSnobal Energy Balance Snow Model." *Water Resources Research* 54, no. 10: 8045–8063. https://doi.org/10.1029/2018WR023190.

Hopkinson, C., and C. Barnes. 2022. *Precipitation Gauge and Supplemental Weather Station Data for Three Oldman River Headwater Locations in SW Alberta*. Federated Research Data Repository, Digital Research Alliance of Canada. https://doi.org/10.20383/102.0551.

Hopkinson, C., T. Collins, A. Anderson, J. Pomeroy, and I. Spooner. 2012. "Spatial Snow Depth Assessment Using LiDAR Transect Samples and Public GIS Data Layers in the Elbow River Watershed, Alberta." *Canadian Water Resources Journal/Revue Canadienne Des Ressources Hydriques* 37, no. 2: 69–87. https://doi.org/10.4296/cwrj3702893.

Hopkinson, C., M. Demuth, M. Sitar, and L. Chasmer. 2001. "Applications of Airborne LiDAR Mapping in Glacierised Mountainous Terrain. IGARSS 2001. Scanning the Present and Resolving the Future." In *Proceedings of the IEEE 2001 International Geoscience and Remote Sensing Symposium* (Cat. No.01CH37217).

Hopkinson, C., M. Hayashi, and D. Peddle. 2009. "Comparing Alpine Watershed Attributes From LiDAR, Photogrammetric, and Contour-Based Digital Elevation Models." *Hydrological Processes* 23, no. 3: 451–463. https://doi.org/10.1002/hyp.7155.

Hopkinson, C., M. Sitar, L. Chasmer, and P. Treitz. 2004. "Mapping Snowpack Depth Beneath Forest Canopies Using Airborne Lidar." *Photogrammetric Engineering & Remote Sensing* 70, no. 3: 323–330. https://doi.org/10.14358/PERS.70.3.323.

Houze, R. A. 2012. "Orographic Effects on Precipitating Clouds." *Reviews of Geophysics* 50, no. 1. https://doi.org/10.1029/2011RG000365.

Jean, M., and E. Davies. 2015. "Water Managers' Perspectives on Reservoir Operations for Sustainable Irrigation in Alberta." *WIT Transactions on Ecology and the Environment* 197: 161–172.

Jeong, H.-G., J.-B. Ahn, J. Lee, K.-M. Shim, and M.-P. Jung. 2020. "Improvement of Daily Precipitation Estimations Using PRISM With Inverse-Distance Weighting." *Theoretical and Applied Climatology* 139, no. 3: 923–934. https://doi.org/10.1007/s00704-019-03012-6.

Kinar, N. J., and J. W. Pomeroy. 2015. "Measurement of the Physical Properties of the Snowpack." *Reviews of Geophysics* 53, no. 2: 481–544. https://doi.org/10.1002/2015RG000481.

Kochendorfer, J., R. Nitu, M. Wolff, et al. 2017. "Analysis of Single-Alter-Shielded and Unshielded Measurements of Mixed and Solid

Precipitation From WMO-SPICE." *Hydrology and Earth System Sciences* 21: 3525–3542.

Kochendorfer, J., R. Rasmussen, M. Wolff, et al. 2017. "The Quantification and Correction of Wind-Induced Precipitation Measurement Errors." *Hydrology and Earth System Sciences* 21, no. 4: 1973–1989.

Leeper, R. D., M. A. Palecki, and E. Davis. 2015. "Methods to Calculate Precipitation From Weighing-Bucket Gauges With Redundant Depth Measurements." *Journal of Atmospheric and Oceanic Technology* 32, no. 6: 1179–1190. https://doi.org/10.1175/jtech-d-14-00185.1.

Li, L., and J. W. Pomeroy. 1997. "Estimates of Threshold Wind Speeds for Snow Transport Using Meteorological Data." *Journal of Applied Meteorology* 36, no. 3: 205–213. https://doi.org/10.1175/1520-0450(1997)036<0205:eotwsf>2.0.co;2.

Lo, Y.-H., J. A. Blanco, B. Seely, C. Welham, and J. P. Kimmins. 2011. "Generating Reliable Meteorological Data in Mountainous Areas With Scarce Presence of Weather Records: The Performance of MTCLIM in Interior British Columbia, Canada." *Environmental Modelling & Software* 26, no. 5: 644–657. https://doi.org/10.1016/j.envsoft.2010.11.005.

Luce, C. H., J. T. Abatzoglou, and Z. A. Holden. 2013. "The Missing Mountain Water: Slower Westerlies Decrease Orographic Enhancement in the Pacific Northwest USA." *Science* 342, no. 6164: 1360–1364. https://doi.org/10.1126/science.1242335.

Lundquist, J. D., M. Hughes, B. Henn, et al. 2015. "High-Elevation Precipitation Patterns: Using Snow Measurements to Assess Daily Gridded Datasets Across the Sierra Nevada, California." *Journal of Hydrometeorology* 16, no. 4: 1773–1792. https://doi.org/10.1175/JHM-D-15-0019.1.

MacDonald, M. K., J. W. Pomeroy, and R. L. H. Essery. 2018. "Water and Energy Fluxes Over Northern Prairies as Affected by Chinook Winds and Winter Precipitation." *Agricultural and Forest Meteorology* 248: 372–385. https://doi.org/10.1016/j.agrformet.2017.10.025.

MacDonald, M. K., J. W. Pomeroy, and A. Pietroniro. 2010. "On the Importance of Sublimation to an Alpine Snow Mass Balance in the Canadian Rocky Mountains." *Hydrology and Earth System Sciences* 14, no. 7: 1401–1415. https://doi.org/10.5194/hess-14-1401-2010.

MacDonald, R. J., J. M. Byrne, S. Boon, and S. W. Kienzle. 2012. "Modelling the Potential Impacts of Climate Change on Snowpack in the North Saskatchewan River Watershed, Alberta." *Water Resources Management* 26, no. 11: 3053–3076.

MacDonald, R. J., J. M. Byrne, and S. W. Kienzle. 2009. "A Physically Based Daily Hydrometeorological Model for Complex Mountain Terrain." *Journal of Hydrometeorology* 10, no. 6: 1430–1446. https://doi.org/10.1175/2009JHM1093.1.

Marks, D., A. Winstral, M. Reba, J. Pomeroy, and M. Kumar. 2013. "An Evaluation of Methods for Determining During-Storm Precipitation Phase and the Rain/Snow Transition Elevation at the Surface in a Mountain Basin." *Advances in Water Resources* 55: 98–110. https://doi.org/10.1016/j.advwatres.2012.11.012.

McCaffrey, D. R., and C. Hopkinson. 2017. "Assessing Fractional Cover in the Alpine Treeline Ecotone Using the WSL Monoplotting Tool and Airborne Lidar." *Canadian Journal of Remote Sensing* 43, no. 5: 504–512. https://doi.org/10.1080/07038992.2017.1384309.

Mekis, E., N. Donaldson, J. Reid, et al. 2018. "An Overview of Surface-Based Precipitation Observations at Environment and Climate Change Canada." *Atmosphere-Ocean* 56, no. 2: 71–95. https://doi.org/10.1080/07055900.2018.1433627.

Meyer, J., J. Horel, P. Kormos, A. Hedrick, E. Trujillo, and S. M. Skiles. 2023. "Operational Water Forecast Ability of the HRRR-iSnobal Combination: An Evaluation to Adapt Into Production Environments." *Geoscientific Model Development* 16, no. 1: 233–250. https://doi.org/10.5194/gmd-16-233-2023.

Mizukami, N., and S. Perica. 2008. "Spatiotemporal Characteristics of Snowpack Density in the Mountainous Regions of the Western United States." *Journal of Hydrometeorology* 9, no. 6: 1416–1426. https://doi.org/10.1175/2008jhm981.1.

Mott, R., D. Scipión, M. Schneebeli, N. Dawes, A. Berne, and M. Lehning. 2014. "Orographic Effects on Snow Deposition Patterns in Mountainous Terrain." *Journal of Geophysical Research: Atmospheres* 119, no. 3: 1419–1439. https://doi.org/10.1002/2013JD019880.

Mott, R., V. Vionnet, and T. Grünewald. 2018. "The Seasonal Snow Cover Dynamics: Review on Wind-Driven Coupling Processes." *Frontiers in Earth Science* 6, no. 197 (December): 197. https://doi.org/10.3389/feart.2018.00197.

Musselman, K. N., N. Addor, J. A. Vano, and N. P. Molotch. 2021. "Winter Melt Trends Portend Widespread Declines in Snow Water Resources. Nature." *Climate Change* 11, no. 5: 418–424. https://doi.org/10.1038/s41558-021-01014-9.

Naderpour, R., M. Schwank, and C. Mätzler. 2017. "Davos-Laret Remote Sensing Field Laboratory: 2016/2017 Winter Season L-Band Measurements Data-Processing and Analysis." *Remote Sensing* 9, no. 11: 1185. http://www.mdpi.com/2072-4292/9/11/1185.

Newton, B. W., B. Farjad, and J. F. Orwin. 2021. "Spatial and Temporal Shifts in Historic and Future Temperature and Precipitation Patterns Related to Snow Accumulation and Melt Regimes in Alberta, Canada." *Water* 13, no. 8: 1013. https://www.mdpi.com/2073-4441/13/8/1013.

Nitu, R. 2010. "CIMO Survey on National Summaries of Methods and Instruments for Solid Precipitation Measurement at Automatic Weather Stations." *International Organization for Migration* 102: TD1544.

OTT Hydromet GmbH. 2019. "Operating Instructions OTT Pluvio2 Precipitation Gauge." OTT Hydromet GmbH. https://www.ott.com/products/accessories-109/ott-pluvio2-weighing-rain-gauge-963/.

Painter, T. H., D. F. Berisford, J. W. Boardman, et al. 2016. "The Airborne Snow Observatory: Fusion of Scanning Lidar, Imaging Spectrometer, and Physically-Based Modeling for Mapping Snow Water Equivalent and Snow Albedo." *Remote Sensing of Environment* 184: 139–152. https://doi.org/10.1016/j.rse.2016.06.018.

Pan, X., D. Yang, Y. Li, et al. 2016. "Bias Corrections of Precipitation Measurements Across Experimental Sites in Different Ecoclimatic Regions of Western Canada." *Cryosphere* 10, no. 5: 2347–2360.

Peixeiro, M. 2022. *Time Series Forecasting in Python*. Shelter Island, NY: United States of America.

Pickering, R. 2018. "Snow Surveying Field Sampling Protocols." Alberta Environment and Parks. http://environmentalmonitoring.alberta.ca/resources/standards-and-protocols/.

Pomeroy, J. W., D. M. Gray, K. R. Shook, et al. 1998. "An Evaluation of Snow Accumulation and Ablation Processes for Land Surface Modelling." *Hydrological Processes* 12, no. 15: 2339–2367. https://doi.org/10.1002/(SICI)1099-1085(199812)12:15<2339::AID-HYP800>3.0.CO;2-L.

Raleigh, M. S., and E. E. Small. 2017. "Snowpack Density Modeling Is the Primary Source of Uncertainty When Mapping Basin-Wide SWE With Lidar." *Geophysical Research Letters* 44, no. 8: 3700–3709. https://doi.org/10.1002/2016GL071999.

Rasmussen, R., B. Baker, J. Kochendorfer, et al. 2012. "How Well Are we Measuring Snow: The NOAA/FAA/NCAR Winter Precipitation Test Bed." *Bulletin of the American Meteorological Society* 93, no. 6: 811–829. https://doi.org/10.1175/bams-d-11-00052.1.

Reba, M. L., J. Pomeroy, D. Marks, and T. E. Link. 2012. "Estimating Surface Sublimation Losses From Snowpacks in a Mountain Catchment Using Eddy Covariance and Turbulent Transfer Calculations." *Hydrological Processes* 26, no. 24: 3699–3711. https://doi.org/10.1002/hyp.8372.

Roe, G. H. 2005. "Orographic Precipitation." *Annual Review of Earth and Planetary Sciences* 33, no. 1: 645–671. https://doi.org/10.1146/annurev.earth.33.092203.122541.

Roe, G. H., and M. B. Baker. 2006. "Microphysical and Geometrical Controls on the Pattern of Orographic Precipitation." *Journal of the Atmospheric Sciences* 63, no. 3: 861–880. https://doi.org/10.1175/jas3619.1.

Ross, A., C. D. Smith, and A. Barr. 2020. "An Improved Post-Processing Technique for Automatic Precipitation Gauge Time Series." *Atmospheric Measurement Techniques* 13, no. 6: 2979–2994. https://doi.org/10.5194/amt-13-2979-2020.

Rotunno, R., and R. A. Houze. 2007. "Lessons on Orographic Precipitation From the Mesoscale Alpine Programme." *Quarterly Journal of the Royal Meteorological Society* 133, no. 625: 811–830. https://doi.org/10.1002/qj.67.

Rutledge, S. A., and P. Hobbs. 1983. "The Mesoscale and Microscale Structure and Organization of Clouds and Precipitation in Midlatitude Cyclones. VIII: A Model for the 'Seeder-Feeder' Process in Warm-Frontal Rainbands." *Journal of the Atmospheric Sciences* 40, no. 5: 1185–1206.

Schindler, D. W., and W. F. Donahue. 2006. "An Impending Water Crisis in Canada's Western Prairie Provinces." *Proceedings of the National Academy of Sciences* 103, no. 19: 7210–7216. https://doi.org/10.1073/pnas.0601568103.

Sexstone, G. A., D. W. Clow, S. R. Fassnacht, et al. 2018. "Snow Sublimation in Mountain Environments and Its Sensitivity to Forest Disturbance and Climate Warming." *Water Resources Research* 54, no. 2: 1191–1211. https://doi.org/10.1002/2017WR021172.

Shook, K., and J. Pomeroy. 2012. "Changes in the Hydrological Character of Rainfall on the Canadian Prairies." *Hydrological Processes* 26, no. 12: 1752–1766. https://doi.org/10.1002/hyp.9383.

Siler, N., C. Proistosescu, and S. Po-Chedley. 2019. "Natural Variability Has Slowed the Decline in Western U.S. Snowpack Since the 1980s." *Geophysical Research Letters* 46, no. 1: 346–355. https://doi.org/10.1029/2018GL081080.

Smith, C. D., A. Ross, J. Kochendorfer, et al. 2020. "Evaluation of the WMO Solid Precipitation Intercomparison Experiment (SPICE) Transfer Functions for Adjusting the Wind Bias in Solid Precipitation Measurements." *Hydrology and Earth System Sciences* 24, no. 8: 4025–4043. https://doi.org/10.5194/hess-24-4025-2020.

Smith, R. 1981. "The Influence of Mountains on the Atmosphere: Recent Advances." *Nowcasting: Mesoscale Observations and Short-Range Prediction* 165: 37.

Smith, R. B. 2019. "100 Years of Progress on Mountain Meteorology Research." *Meteorological Monographs* 59: 20.21–20.73.

Thakur, P. K., S. P. Aggarwal, G. Arun, et al. 2017. "Estimation of Snow Cover Area, Snow Physical Properties and Glacier Classification in Parts of Western Himalayas Using C-Band SAR Data." *Journal of the Indian Society of Remote Sensing* 45, no. 3 (June): 525–539. https://doi.org/10.1007/s12524-016-0609-y.

Thiessen, A. H. 1911. "Precipitation Averages for Large Areas." *Monthly Weather Review* 39, no. 7: 1082–1089. https://doi.org/10.1175/1520-0493(1911)39<1082b:PAFLA>2.0.CO;2.

USDA, & NRCS. 2007. "Statistical Techniques Used in the VIPER Water Supply Forecasting Software." Electronic Directives System, Technical Notes, Snow Survey and Water Supply Forecasting, Natural Resources Conservation Service, U.S. Department of Agriculture. https://www.nrcs.usda.gov/programs-initiatives/sswsf-snow-survey-and-water-supply-forecasting-program/water-supply.

Veatch, W., P. D. Brooks, J. R. Gustafson, and N. P. Molotch. 2009. "Quantifying the Effects of Forest Canopy Cover on Net Snow Accumulation at a Continental, Mid-Latitude Site." *Ecohydrology* 2, no. 2: 115–128. https://doi.org/10.1002/eco.45.

Waterton Lakes National Park. 2017. *Kenow Fire: Burn Severity Map*, 1. Gatineau, Canada: Parks Canada National Office. https://www.pc.gc.ca/en/pn-np/ab/waterton/nature/environment/feu-fire/feu-fire-kenow/brulage-burn.

Wolff, M., K. Isaksen, A. Petersen-Øverleir, K. Ødemark, T. Reitan, and R. Brækkan. 2015. "Derivation of a New Continuous Adjustment Function for Correcting Wind-Induced Loss of Solid Precipitation: Results of a Norwegian Field Study." *Hydrology and Earth System Sciences* 19, no. 2: 951–967.

Wright, R. 2021. "Weighing Gauge Time Series Analysis and Noise Filtering Tool." In Alberta Agriculture and Forestry.

Wright, R. 2024. "Current and Historical Alberta Weather Station Data." Alberta Climate Information Service (ACIS). https://www.acis.alberta.ca/acis/app/resources/Alberta-Climate-Information-Service_(ACIS)-Definitions_y2024_m02_d06.pdf.

Yang, D., D. Kane, Z. Zhang, D. Legates, and B. Goodison. 2005. "Bias Corrections of Long-Term (1973–2004) Daily Precipitation Data Over the Northern Regions." *Geophysical Research Letters* 32, no. 19. https://doi.org/10.1029/2005GL024057.

Zahmatkesh, Z., S. Kumar Jha, P. Coulibaly, and T. Stadnyk. 2019. "An Overview of River Flood Forecasting Procedures in Canadian Watersheds." *Canadian Water Resources Journal/Revue Canadienne Des Ressources Hydriques* 44, no. 3: 213–229. https://doi.org/10.1080/07011784.2019.1601598.

Zhang, L., L. Zhao, C. Xie, et al. 2015. "Intercomparison of Solid Precipitation Derived From the Weighting Rain Gauge and Optical Instruments in the Interior Qinghai-Tibetan Plateau." *Advances in Meteorology* 11: 936724. https://doi.org/10.1155/2015/936724.

Zhang, Z., S. Glaser, R. Bales, M. Conklin, R. Rice, and D. Marks. 2017. "Insights Into Mountain Precipitation and Snowpack From a Basin-Scale Wireless-Sensor Network." *Water Resources Research* 53, no. 8: 6626–6641. https://doi.org/10.1002/2016WR018825.

Appendix A

AEPA Field Snow Sampling

The four AEPA field snow sampling locations are shown in Figure A1. Figure A2 shows SWE measurements recorded by the AEPA Gardiner snow water (snow pillow) sensor in the subalpine just north of WCW. The Gardiner sensor recorded 665 mm for the 5 Mar 2020 whereas the 4 Mar 2021 measured less than half the snow water at 325 mm. Figure A3 shows the 30-year AEPA field snow sampling density boxplots for WC II, Akamina, SRHC and Gardiner.

AEPA Field Snow Sampling Locations

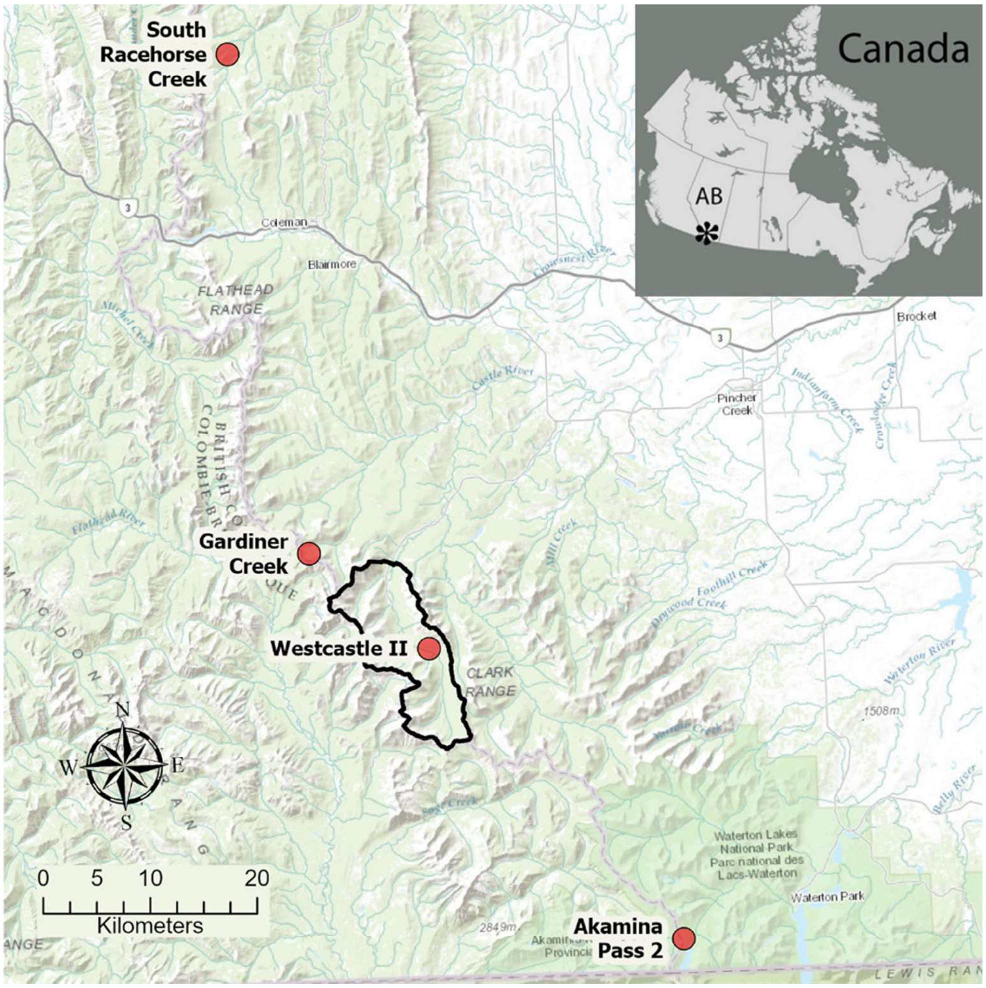

FIGURE A1 | Southwestern Alberta. Red dots are AEPA field snow sampling sites. The black outline is the West Castle Watershed. South Racehorse Creek (SRHC (1920 m.asl)); Gardiner Creek (Gardiner (1940 m.asl)); WC II (West Castle II (1533 m.asl)); Akamina Pass 2 (Akamina (1809 m.asl)). Inset: Star showing the study location within Alberta, Canada.

AEPA Snow Density

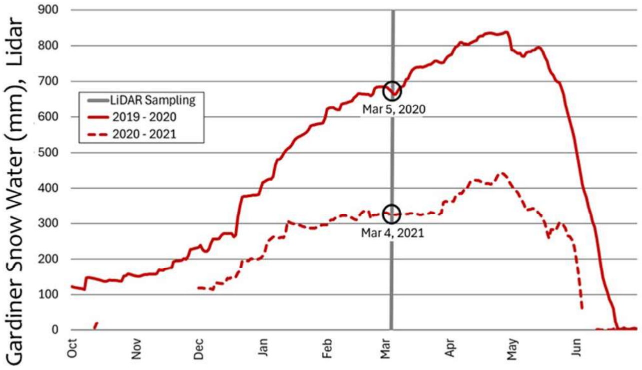

FIGURE A2 | AEPA Gardiner (1940 m.asl) Snow Water (measured using the snow pillow sensor) for each lidar mission date (highlighted by the black circle) shows continuous SWE conditions in the subalpine just north of WCW.

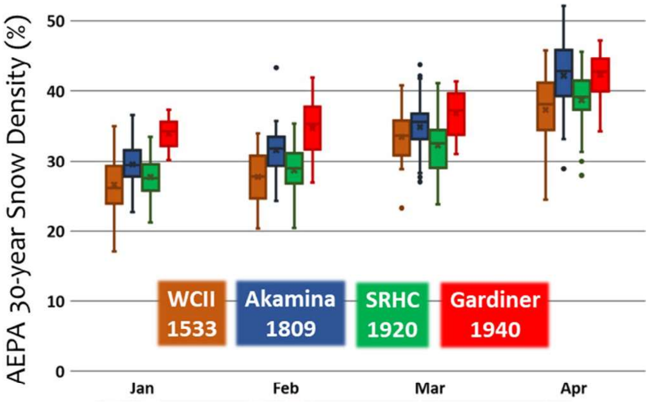

FIGURE A3 | AEPA field snow sampling density for WC II, Akamina, SRHC, and Gardiner. Snow density was expressed as a percentage of water equivalent (standard water density is 1000 kg/m^3). This approach was used to derive watershed wide spatialized modelled SWE estimates (calculated by multiplying snow depth and snow density). Box and Whisker, X is mean, bar is median, top and bottom T are the range, coloured box is the interquartile range (quartile 1–quartile 3). Outliers are the dots outside the T (any value that is above or below 1.5 times the interquartile range).

ULAL Field Snow Sampling for AEPA Model Verification

Figure A4 shows locations within WCW where ULAL team members conducted field snow sampling during March 2019 as well as coincident with the 5 March 2020 and 5 March 2021 lidar snow sampling flights.

Table A1 shows ULAL field snow densities sampled within WCW in March 2019, March 2020 and March 2021. ULAL sampling ULAL sampling for 2019 was done on at CMR as well as in the valley at the bottom of the mountain. The mean snow density (expressed as %) for CMR (range of 21–36) was 8% higher than at the valley (range of 11–27) location. ULAL sampling that was coincident with the lidar flights were used to verify AEPA modelled ranges. Sampling at CMR proved challenging due to snow depths ranging from 0 m to beyond the depth of a 3 m avalanche probe within a 25 m radius of the precipitation gauge. At the time of the 5 Mar 2020 lidar flight, thick ice lenses were present within the snowpack making it difficult to sample the full depth for SWE and density. It was only possible to collect 3 snow measurements (snow density of 32, 35 and 49) in shallower and packed snow. CMR measured snow densities were within the AEPA March 1 historic range of 0.26–0.35 (mean ± one standard deviation) used for the snow density model. No field snow sampling was done at CMR for the 4 Mar 2021 lidar flight. ULAL data were not assumed to be a valid source of reference data to drive the snow density model in the alpine zone since there were not enough spatial and temporal data points to quantify the central tendency at any site. These data were intended to complement the long term AEPA data record.

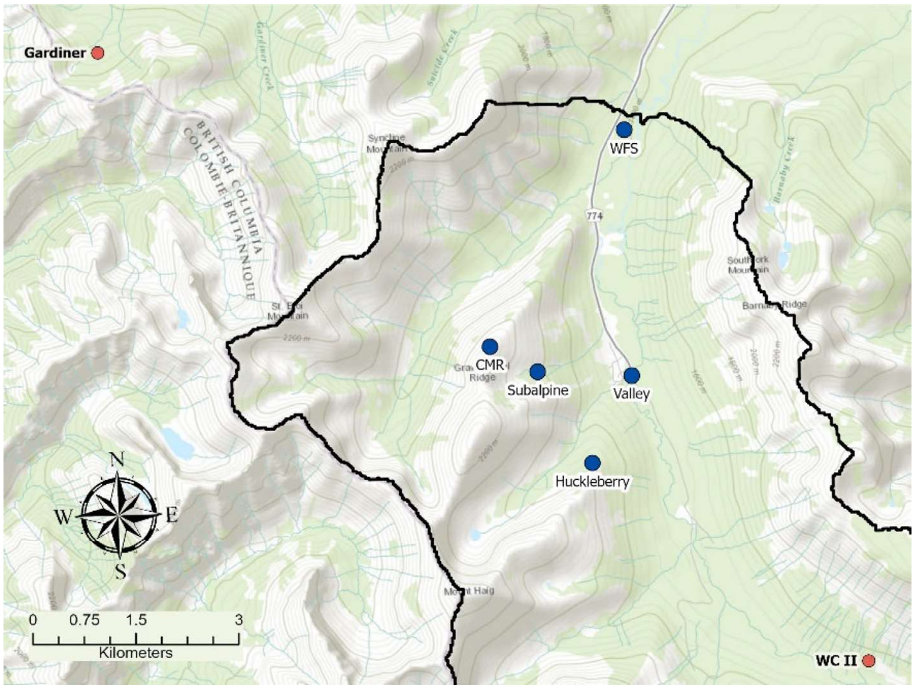

FIGURE A4 | West Castle Watershed Field Snow Sampling Sites. Red dots are AEPA field snow sampling sites. The black outline is the upper portion of the West Castle Watershed. Gardiner Creek (Gardiner (1940 m.asl)); WC II (West Castle II (1533 m.asl)); WFS (Westcastle Field Station (1403 m.asl)); Valley (1403 m.asl); Subalpine (1850 m.asl); Huckleberry (1754 m.asl) and CMR (Castle Mountain Ridge (2136 m.asl)).

TABLE A1 | ULAL field snow sampling density. Snow density was computed using SWE divided by snow depth for each observation in the sample set and expressed as the percentage of standard liquid water equivalent instead of kg/m^3. Max, Min, Mean, Median, StDev and *n* (the count of the number of samples) are presented for 16 March 2019, and sampling coincident with the 5 March 2020 and 4 March 2021 lidar snow sampling flights.

Date	Elev	Location	Max	Min	Mean	Median	StDev	*n*
2019-03-16	1403	Valley	27	11	20	21	5	6
2019-03-16	2136	CMR	36	21	28	30	6	5
2020-03-05	1403	WFS	32	23	28	29	4	5
2020-03-05	2136	CMR	49	32	39	35	10	3
2021-03-05	1403	WFS	35	20	29	28	5	12
2021-03-05	1754	Huckleberry	33	30	32	31	1	5

Appendix B

WCW Images of Snowpack Conditions

On 16 March 2019, photos and snow depth measurements were taken at CMR (Figure B1), a subalpine site (Figure B2) and WFS (Figure B3) to illustrate depth variability in WCW at valley, subalpine and ridge locations.

FIGURE B1 | CMR elevation 2130 m.asl. This image shows areas with scoured (no snow) portions of the alpine ridge to shallow snowpacks. Several depth measurements were taken in this location (where there was snow) ranging from 0.33 to 1.59 m.

FIGURE B2 | Subalpine elevation 1850 m.asl (Figure A4 shows the location of this subalpine site). The avalanche probe seen on the bottom right of the image was 2.55 m. Several depth measurements were taken at this location, ranging from 1.94 to 2.85 m.

FIGURE B3 | WFS elevation 1403 m.asl. The WFS field station can be seen in the top left side of the image. The weather station is on the right centre of the image. Several snow depth measurements were taken in this location ranging from 0.31 to 1.08 m.